Geothermal Engineering Integrating Mitigation of Induced Seismicity in Reservoirs

Proposal acronym: GEISER
Type of funding scheme: Collaborative Project
Work programme topics addressed: ENERGY.2009.2.4.1
Call Selected: FP7-ENERGY-2009-1

Work Package 4
Task 4.1:
Role of pore pressure changes

Deliverable D4.3 - Final Report

December, 2011

With the contribution of:

GFZ	Elli-Maria CHARALAMPIDOU, Georg DRESEN
BRGM	Xavier RACHEZ
ISOR	Kristján AGUSTSSON, Ólafur G. FLOVENZ
TNO	Brecht WASSING, Tanneke OUBOTER, Jan-Diederick VAN WEES
GEOWATT	Martin SCHOENBALL, Clément BEAUJARD, Thomas KOHL
ARMINES	Dominique BRUEL
INGV	Giuseppe DE NATALE, Antonio TROIANO, Maria Giulia DI GIUSEPPE, Anna TRAMELLI, Claudia TROISE

Synopsis

The WP4 work package is dedicated to understanding the geomechanicalcauses and processes of induced seismicity in various contexts and at various scales. Different modeling approaches and laboratory experiments have been performed to investigate some of the key factors influencing induced seismicity: the goal is to develop physical concepts to help explain the interaction of pore-pressure changes, temperature decrease, fault activation (including dynamic rupture) and seismic event magnitudes.

This report corresponds to the deliverable D4.3 for the GEISER project. It gathers the work performed by the different partners within task 4.1, referred to as “Role of pore pressure changes”:

- The laboratory experiments performed by GFZ on the monitoring of induced micro-seismicity from fluid injections,
- The core samples from Icelandic geothermal sites provided by ISOR,
- The study on the structural heterogeneities compartmenting sedimentary reservoirs performed by TNO,
- The study performed by GEOWATT on how the Stress Coulomb changes can be used for assessing seismic hazard,
- The work performed by INGV on time-dependent variation of pore pressure with a fluid dynamic approach.

Contents

1. Monitoring induced micro-seismicity from fluid injection experiments: laboratory scale 11

1.1. PREAMBLE 11

1.2. OBJECTIVES 11

1.3. METHODOLOGY AND EXPERIMENTAL RESULTS 11

1.3.1. Tested material and experiments procedure 12

1.3.2. Experimental methods 13

1.4. RESULTS 14

1.4.1. Fracturing of dry solid specimens 14

1.4.2. Re-activation of the fracture through fluid injection into dry specimen 19

1.4.3. Re-activation of the fracture through fluid pressure pulse into saturated specimen 26

1.4.4. Re-activation of a pre-cut fracture through fluid pressure increase into saturated specimen 31

1.5. RESULTS 33

1.6. PERSPECTIVES, FOLLOWED-UP EVENTS AND PUBLICATIONS 34

1.7. REFERENCES 34

2. Core Samples for laboratory experiments 37

2.1. PREAMBLE 37

2.2. CORE SAMPLES 37

3. Structural heterogeneities compartmenting sedimentary reservoirs 39

3.1. PREAMBLE 39

3.2. INTRODUCTION 39

3.3. IMPACT OF PORO-ELASTIC STRESS CHANGES AND RESERVOIR COMPARTMENTALIZATION ON FAULT STABILITY 40

3.3.1. Poro-elastic effects of depletion and injection 40

3.3.2. Geometrical effects of depletion of and injection into a sedimentary reservoir 42

3.4. FIELD CASE: INDUCED SEISMICITY CAUSED BY GAS PRODUCTION FROM A COMPARTMENTALIZED RESERVOIR IN THE NORTHERN NETHERLAND 43

3.5. EGS IN COMPARTMENTALIZED SEDIMENTARY RESERVOIR – SOME PRELIMINARY CALCULATIONS 48

3.6. CONCLUSIONS 50

3.7. REFERENCES 51

4. From geomechanical modeling to seismic hazard assessments 53

4.1. PREAMBLE 53

4.2. INTRODUCTOIN 53

4.3. GEOMECHANICAL MODELLING 53

4.4. RATE-AND-STATE MODEL 53

4.5. RESULTS 54

4.5.1. Application to the Stimulation of GPK4 at Soultz-sous-Forêts (France) .. 54

4.5.2. Different stimulation scenarios 55

4.5.3. Interpretation 56

4.6. CHALLENGES 56

4.7. REFERENCES 56

5. Time-dependent variation of pore pressure with a fluid dynamic approach 57

5.1. PREAMBLE 57

5.2. INTRODUCTION 57

5.3. METHOD 57

5.4. RESULTS 58

5.5. CONCLUSIONS..59

5.6. REFERENCES 64

List of illustrations

Figure 1: Source types and hypocentre locations from dry specimen Fb34. a) Pre-failure, stress hardening up to peak stress; b) Pre-failure, onset of axial stress softening after the peak stress; c) Failure, stress drop; d) Post-failure. AE events with amplitudes higher than 1000 µVolts are plotted. 16

Figure 2: Source types and hypocentre locations from dry specimen Fb34 during the fault evolution. AE events with amplitude higher than 1000 µVolts are shown in circles, while AE events with amplitudes higher than 3162 µVolts are shown in diamonds. T-, S-, and C-type events are illustrated in green-blue and red colors. 17

Figure 3: Source type and hypocentre locations from dry specimen Fb35. a) Pre-failure, stress hardening up to peak stress; b) Pre-failure, onset of axial stress softening after the peak stress; c) Failure, stress drop; d) Post-failure. AE events with amplitudes higher than 1000 µVolts are plotted. 18

Figure 4: Source types and hypocentre locations during the distilled water injection into the dry specimen Fb35. a) Constant axial force stage; b) Constant axial force stage, onset of 5 ml/min inlet flow rate, change in velocities of sensors glued at z=+22.5 mm and z=+42.5 mm from the bottom of the specimen; c) Failure, 5 ml/min inlet flow rate; d) Constant displacement of piston stage, 5 ml/min inlet flow rate; e) Constant piston position stage, 5 ml/min inlet flow rate, change in velocities of sensors glued at z=+62.5 mm and z=+82.5 mm from the bottom of the specimen; f) Constant piston position stage, 5 ml/min inlet flow rate, change in velocities of sensors glued at z=+102.5 mm from the bottom of the specimen. AE events with amplitudes higher than 316 µVolts are plotted. T-, S-, and C-type events are shown in green, blue and red, respectively. 20

Figure 5: Source types and hypocentre locations during water injection in dry specimen Fb35. AE events with amplitudes higher than 316 µVolts are shown in small circles. AE events with amplitudes higher than 1000 µVolts are visualised in big circles, while AE events with amplitudes higher than 3162 µVolts are shown in diamonds. T-, S-, and C-type events are illustrated in green-blue and red colours. 22

Figure 6: Specimen Fb35: source types and hypocentre locations during the failure of the re-activated fault. a) AEs with amplitude higher than 316 µVolts ; b) AEs with amplitude higher than 1000 μVolts ;c) AEs with amplitude higher than 3162 μVolts. T-, S-, and C-type events are shown in green, blue and red, respectively. 23

Figure 7: Source types and hypocentre locations during the distilled water injection into the dry specimen Fb34. a) Constant axial force stage, inlet pore pressure equals to 5 MPa, change in velocities of sensors glued at z=+22.5 mm; b) Constant axial force stage, inlet pore pressure equals to 5 MPa, change in velocities of sensors glued at z=+42.5 mm; c) Constant axial force stage, inlet pore pressure equals to 5 MPa, change in velocities of sensors glued at z=+62.5 mm; d) Constant axial force stage, inlet pore pressure equals to 5 MPa, change in velocities of sensors glued at z=+82.5 mm. AE events with amplitudes higher than 1000 μVolts are plotted. T-, S-, and C-type events are shown in green, blue and red, respectively. 24

Figure 8: Source types and hypocentre locations from dry specimen Fb34 during water injection. AE events with amplitudes higher than 1000 μVolts are visualised in circles, while AE events with amplitudes higher than 3162 μVolts are shown in diamonds. T-, S-, and C-type events are illustrated in green-blue and red colours. 25

Figure 9: Saturated specimen Fb34: source types and hypocentre locations during the failure of the re-activated fault. a) AE events with amplitude higher than 316 μVolts ; b) AE events with amplitude higher than 1000 μVolts; c) AE events with amplitude higher than 3162 μVolts. T-, S-, and C-type events are shown in green, blue and red, respectively. 27

Figure 10: Source types and hypocentre locations from saturated specimen Fb34 during water injection. AE events with amplitudes higher than 316 μVolts are visualised in circles, while AE events with amplitudes higher than 1000 μVolts are shown in diamonds. T-, S-, and C-type events are illustrated in green-blue and red colours. 28

Figure 11: Saturated specimen Fb34: source types and hypocentre locations during the failure of the re-activated fault. a) AE events with amplitude higher than 316 μVolts ; b) AE events with amplitude higher than 1000 μVolts; c) AE events with amplitude higher than 3162 μVolts. T-, S-, and C-type events are shown in green, blue and red, respectively. 29

Figure 12: Source types and hypocentre locations from saturated specimen Fb34 during water injection. AE events with amplitudes higher than 316 μVolts are visualised in circles, while AE events with amplitudes higher than 1000 μVolts are shown in diamonds. T-, S-, and C-type events are illustrated in green-blue and red colours. 30

Figure 13: Source types and hypocentre locations from saturated specimen FL1 before (a), during (b) and after (c) the saw-cut plane re-activation due to increasing pore pressure. AE events with amplitude higher than 316 μVolts are shown in circles. T-, S-, and C-type events are illustrated in green-blue and red colours. 31

Figure 14: Source types and hypocentre locations from saturated specimen FL1 during the saw-cut plane re-activation. AE events with amplitude higher than 316 μVolts are shown in circles, while AE events with amplitudes higher than 1000 μVolts are shown in diamonds. T-, S-, and C-type events are illustrated in green-blue and red colours. 32

Figure 15 : The Reykjanes geothermal field. The location of the wells is marked with red circle. Well RN-17B is vertical and the track of well RN-30 is shown with a gray line. Red areas show postglacial eruption sites and yellow and pink denote areas of thermal alteration. 37

Figure 16 : Stress paths on a critically oriented fault plane during reservoir depletion (left) and injection into a reservoir (right). Initial tectonic setting is extensional (S_V> S_{Hmax}> S_{hmin}). Upper figures show horizontal ($S_{h'}$) and vertical effective stress ($S_{v'}$), shear (t_s) and normal tractions (t'_n) on a critically oriented faultplane with dip α and the related Mohr circle for stress and Mohr failure envelope (φ is friction coefficient of the fault). Middle graph left shows stress path on the faultplane during depletion, which is critical (converging on the MC-line). Middle graph right shows stress path on the fault plane during injection which is non-critical (diverging from the MC-line). Lower graph left shows stress path on the faultplane during depletion (non-critical). Lower graph right shows stress path on the faultplane during injection (critical). Subscript 0 means initial stress, subscripts dep and inj mean stresses after depletion resp. injection. 41

Figure 17 : Impact of injection of water into an open fracture / open fault in an impermeable or low permeable rock mass. Due to the pore pressure increase the Mohr circle shifts towards the left and normal effective stresses on the fracture decrease, resulting in potential fracture/fault reactivation. This is regarded the dominant mechanism for fracture reactivation in EGS in non-sedimentary, low permeability fractured reservoirs. 42

Figure 18 : Geometrical effects on differential compaction, fault shear tractions and the potential of fault reactivation. 43

Figure 19 : Figure 4. Schematical geological model of the Rotliegend sandstone reservoir and location of induced seismicity during gas production. All events are located at the tip of the fault intersecting the reservoir blocks. 44

Figure 20 : Disc-shaped model in DIANA of a sedimentary sandstone reservoir (upper figures, reservoir is presented in green & orange) intersected by a partially sealing normal fault. Upper figures, caprock is shown in yellow and blue). The offset of the southwestern reservoir block and caprock varies along the strike of the fault. The north eastern reservoir block lies horizontally. Lower left graph shows the pore pressure evolution (blue line horizontal reservoir block, brown line dipping reservoir block) during gas production. Red squares present timing and magnitudes of seismic events. 46

Figure 21 : a and b) Modelled fault slip during depletion of the gas field. Largest fault slip occurs at the tip of the fault, at the juxtaposition of the depleted reservoir blocks. This is consistent with the observed seismicity during depletion, which is localized at the tip of the fault. c and d) Area of reactivated fault patches presented in red. 47

Figure 22 : Left: a) and b) are locations of monitoring points on the central fault plane. Both the intersection of the horizontal and the dipping reservoir block are projected on the faultplane. Right: Stress paths on central faultplane in the disc shaped model. Stress paths intersect the MC failure envelope of the fault during depletion, which means at the location of the monitoring points the fault is reactivated. 47

Figure 23 : Stress path on critically oriented fault plane during water injection (pore pressure increase) in a compressional tectonic setting ($S_{Hmax}>S_{hmin}>S_v$). 49

Figure 24 : Schematic 2D FE model of a 200m-thick sandstone reservoir at a depth of approximately 3km, intersected by a reverse fault. The fault is modelled by interface elements with a Mohr-Coulomb failure criterion (friction coefficient 0.6, no cohesion). The reservoir and the surrounding rocks are assumed elastic. 49

Figure 25 : Stress path in monitoring points a and b on fault plane due to pore pressure increase in individual reservoir compartments and both reservoir compartments simultaneously. For location of monitoring points see Figure 24. 50

Figure 26 : (a) Injection rates during the GPK4 stimulation and downhole pressure simulated with HEX-S. (b) Seismicity rates converted from pore pressures for two $A\sigma$. 54

Figure 27 : (a) Estimated seismicity rates and cumulative rates, compared to (b) observed seismicity during the stimulation of GPK4. The simulated temporal evolution of cumulative seismicity rates are in good agreement with the observation. 54

Figure 28 : Theoretical model meshes; a) Axial symmetric model domains used for thermo-fluid dynamical modeling and for surface deformation computation. Right side: finite-difference computational domain for thermo-fluid dynamical modeling. The green part of the model is characterized by a permeability 10^{-14} m^2, while the external part has a permeability 10^{-16} m^2; b) Initial conditions for Pressure (P) and Temperature (T), at the top of the model, Temperature and Pressure are fixed at atmospheric values, while on the bottom the pressure is lithostatic, with average density r=2500 kg/m^3, while the Temperature is fixed at a value of 300°C. 60

Figure 29: Pressure changes (left) and maximum Coulomb stress changes (right) resulting from injection (upper) and withdrawal (lower) of 50 l/s of water, at 5 km of depth, in a homogeneous medium with permeability 10^{-16} m^2. It is evident that the pressure changes induced by water injection and withdrawal are quite similar apart from the sign. The Coulomb stress patterns show, on the contrary, strong differences. The discriminating factor is that, for withdrawal, the normal component in the Coulomb stress equation is decreased, thus stabilizing the fractures, and the only positive effect occurs where additional shear stress is generated. Water injection, on the contrary, increases the normal component in the volume around, thus destabilizing the fractures at a much larger extent. 61

Figure 30 : Simplified stimulation functions for GPK2 and GPK3 Soultz-sous-Forêts wells (left), and sketch of simulation volume with wells positions and pressure/temperature initial conditions (right). 62

Figure 31 : Estimated pressure changes for the different phases of the injection experiment described in Figure 30 Numbers from 1 to 6 refer to the times of the stimulation cycle shown in Figure 30. 63

Figure 32 : Maximum Coulomb stress changes for the different phases of the injection experiment described in Figure 30. 63

Figure 33: Results (projected on map at 5000 m of depth) for pressure and maximum Coulomb stress changes after the first three days of stimulation of GPK3 well. The reference system is rotated along the direction passing between the two wells. Coulomb stress changes are also compared with seismicity occurred in the period 0-3 days. Note the good agreement between positive stress changes and seismic areas.................... 63

Figure 34 : Results (projected on map at 5000 m of depth) for pressure and maximum Coulomb stress changes after the end of stimulation cycle of the two wells. Coulomb stress changes are also compared with seismicity occurred in the period 0-3 days. Note, also in this case, the good agreement between positive stress changes and seismic areas. 64

1. Monitoring induced micro-seismicity from fluid injection experiments: laboratory scale

1.1. PREAMBLE

The role of GFZ in Task 4.1 is to conduct laboratory experiments coupled with Acoustic Emission monitoring during different fluid injection scenarios. Results of 4D acoustic emissions are presented in this section 1. Pre-existing fractures were re-activated by pore pressure changes and fluid pressure perturbations in dry and saturated sandstone specimens.

1.2. OBJECTIVES

Laboratory experiments, which have been carried out at GFZ, aimed at a better understanding of the basic physical micro-mechanisms that might induce micro-seismicity by fluid injection at rock specimens deformed at the laboratory scale (from cm to µm scale). Factors such as the pore pressure changes, the flow rate and the injection duration as well as the fracture properties and the in situ stress states have been examined. Different injection scenarios causing induced seismicity due to fluid injection have been investigated.

In terms of experimental mechanics, results have been obtained by a combination of a variety of experimental methods. Such experimental procedure is highly recommended at the laboratory scale, especially when each experimental method is sensitive to different parameters. In particular, axial and radial deformations were measured during most of the experiments. These point-wise measurements concern the global deformation throughout the whole or a specific length of the samples. Furthermore, Acoustic Emissions (AE) and ultrasonic velocities were monitored in situ. Ultrasonic measurements are sensitive to the damage processes. Different source type events together with accurate AE hypocentre locations (accuracy of 2 mm) could describe the actual micro-mechanisms induced by fluid injection. X-ray computed tomography, which is preliminary sensitive to density variations (when the photon energy and the atomic number of the material are constant), was also applied either before or after the laboratory deformation of the rock specimens.

1.3. METHODOLOGY AND EXPERIMENTAL RESULTS

In this section, the tested material, the experimental procedure and the experimental methods are discussed [sections 1.3.1 and 1.3.2]. Results have been grouped in four sections and they describe the processes involved in the fracturing of dry solid specimens [section 1.4.1, specimens FB34, Fb35], the re-activation of a fracture through fluid injection into dry specimens [section 1.4.2, specimens FB34, Fb35], the re-activation of a fracture through fluid pressure pulse into saturated specimens [section 1.4.3, specimen FB34] and re-activation of a pre-cut fracture through fluid pressure increase into a saturated specimen [section 1.4.4, specimens FL1]. The main conclusions of the discussed results, which focus on the quantification of the micro-mechanisms involved during fluid injections, are drawn [section 1.5].

1.3.1. Testedmaterial and experimentsprocedure

The Flechtingen sandstone (Flechtigenquary, NE Germany) was used during this experimental study. The mineralogical composition of this Lower Permian rock [Ellenberg et al., 1976] consists of 65-75% quartz, and 15% of calcite and illite [Zang et al., 1996]. The mean grain size of quartz grains is between 0.1 and 0.5 mm, the initial porosity varies between 5.5% and 9%, and the permeability is of the order of 10^{-16} to 10^{-17} m^2 [Stanchits et al., 2011]. Eight cylindrical specimens of 50 mm diameter and length of 100, 120 and 125 mm were cored parallel to bedding.

Two cylindrical specimens were solid rock cylinders (Fb34, Fb35) and six specimens were cut in half along a saw-cut inclined to different orientations to their long axis (FL1, Fl2, Fl3, Fl4, Fl5, Fl6. Note that the three last specimens will be deformed in the following months). Boreholes of 2.5mm were drilled to the bottom part of these specimens to intersect the saw cut surface. The boreholes were parallel to the bedding.

All experiments were carried out in a servo-hydraulic loading frame from Material Testing Systems (MTS) with a load capacity of 4600 kN, at GFZ. In this report, AE results together with source type event identification are presented, from the two solid rock specimens (Fb34, Fb35) and one saw-cut specimen (FL1), to focus on the role of pressure change. Results from the rest saw-cut specimens will be presented in Task 4.3 [Role of faults and fractures], although experimental results from both Task 4.1 and 4.3 are relatively interconnected.

The experimental procedure during the tests presented in Task 4.1 [Role of pore pressure changes] is summarized as following:

1) Dry specimens were loaded under hydrostatic compression at 40 MPa (Fb35, solid) and 80 MPa (Fb34, solid and FL1, saw-cut) confining pressures. The Fb34 (solid) had been previously fractured under triaxial compression at 40 MPa confining pressure.

2) Specimens Fb34 (fractured and ‘locked’ at 80 MPa confining pressure) and FL1 (saw-cut and ‘locked’ at 80 MPa confining pressure) were then loaded under triaxial compression close to the critical stress state, applying a displacement control of 20 μm per minute. Specimen Fb35 (fractured, but not ‘locked’ under hydrostatic compression after the fracture) was directly loaded under triaxial compression (at the same displacement rate) for a short time, because it was already very close to the critical stress state.

(3) The position of the piston applying load to the specimens was held constant for a while, which allowed the samples to creep.

4) The applied axial load was held constant and the position of the piston was kept free to maintain a constant axial force, but restricted to a certain displacement range so as

to avoid any potential big and abrupt displacement, which might totally destroy the tested specimen. The choice of this particular displacement range was not trivial since a relatively narrow range might also lead to restricted sliding of the fault under constant axial force. In this stage distilled water was injected into dry or saturated specimens from the bottom port (bottom boundary of the specimens) by controlling either the inlet pore pressure or the inlet flow rate.

4a) For the case of the dry specimen Fb34 (fractured under triaxial compression at a constant confining pressure of 40 MPa and ‘locked’ at 80 MPa confining pressure) distilled water was pumped through the specimen by applying a constant inlet pore pressure of 5 MPa until the re-activation of the pre-exiting naturally created ‘locked’ fault of the previous stage. Axial force was held constant during the injection. An initial inlet overpressure occurred before pore pressure stabilized to 5 MPa.

4b) For the case of the dry specimen Fb35 (fractured under triaxial compression at 40 MPa constant confining pressure and loaded triaxially slightly after the stress drop had occurred during the fracturing of the previous stage) distilled water was pumped through the specimen by applying a constant inlet flow rate of 5 ml/min until the inlet pore pressure reached a value closed to 5 MPa. The flow rate control at the onset of the injection was applied to avoid as much as possible the sudden inlet overpressure, since this specimen was very close to the critical stress state. The re-activation of the pre-exiting naturally created fault occurred during the constant flow rate and under constant axial force. Further sliding along the fault occurred during the subsequent constant displacement stage of the piston.

4c) For the case of the saturated saw-cut specimen FL1 (‘locked’ under 80 MPa confining pressure, fully saturated with distilled water maintaining 1MPa constant inlet and outlet pore pressure and having a relatively complicated loading history) a relatively small amount of distilled water was pumped through the specimen (4 ml) by keeping a constant inlet flow rate of 0.1 ml/min. Inlet and outlet pore pressures were increased. Axial force was held constant and a very small drop occurred during the re-activation of the saw-cut plane.

5) After the re-activation of the pre-existing naturally created fault, saturated specimen Fb34 was re-loaded twice under triaxial compression close to the critical stress state, at constant confining pressures of 100 and 120 MPa, respectively. The inlet pore pressure was set constant to 25 and 45 MPa, respectively while the axial force was kept constant in order to re-activate the pre-existing faults, this time, in a saturated specimen.

1.3.2. Experimental methods

Fourteen P-wave sensors were glued directly to the surface of the sandstone specimens and sealed in a Neoprene jacket with two-component epoxy. These ultrasonic sensors, which consisted of PZT piezoceramic disks of 5 mm diameter and 2 mm thickness placed on brace housing, had a resonant frequency of 1 MHz. P-wave velocity measurements were made along 50 different traces and AEs were monitored during the experiments. Signals were amplified by 40 dB, using Physical Acoustic

Corporation (PAC) preamplifiers. Half of the sensors that were used for ultrasonic transmission applied 100 Volts electrical pulses every 30 seconds. During the transmission, these sensors were disconnected from the preamplifiers. Full waveforms AE and ultrasonic signals were stored in a 16 channel transient recording system (DAXBox, PRÖKEL, Germany) with an amplitude resolution of 16 bit at 10 MHz sampling rate [Stanchits et al., 2006, 2009]. During the experiments, all ultrasonic signals and AE waveforms were recorded in 8 internal hard disks of the recording system with no dead time between the sequential signals.

After the experiments both ultrasonic signals and AE waveforms were automatically discriminated. The P-wave onset-times were calculated by applying an automatic picking based on the Akaike information criterion [Leonard and Kennett, 1999].The AE hypocentre locations were calculated by minimising the travel time residuals using the downhill simplex algorithm [Nelder and Mead, 1965], considering time-dependent variations in velocities [Stanchits et al., 2006]. The estimated accuracy of the AE hypocentre locations was of 2 mm.

Furthermore, first motion amplitudes were picked automatically and first motion polarities were used to distinguish AE sources in three different groups linked to different mechanisms: tensile, shear and collapse events, according to [Zang et al., 1998]. Source type events were plotted together with the AE hypocentre locations.

X-ray Computed tomography was performed after the experiments. All specimens were X-ray scanned at GFZ in order to better characterise the deformation features and the actual fracture planes. The x-ray images had a voxel size resolution of 30 μm.

1.4. RESULTS

1.4.1. Fracturing of dry solid specimens

Solid specimens Fb34 and Fb35 were fractured during this stage, in order the fractures to be re-activated in the following stages [section 1.4.2,1.4.3] by distilled water injection. Both specimens were initially loaded dry under triaxial compression at 40 MPa confining pressure up to shear failure. AE feedback control of the loading rate was performed during the axial loading [Lockner et al., 1991; Stanchits et al., 2006; Stanchits et al., 2011]. Specimens were initially subjected to 20 μm/min displacement rate, as long as the AE activity was kept relatively low. When AE activity was increased more than a defined threshold level, the displacement rate was decreased, or the piston was retracted and the specimen was unloaded until the AE activity became smaller than the defined threshold level. In such way a more gentle failure of the specimen was achieved [Lockner et al., 1991, 1992, Stanchits et al., 2011].

Figure 1 presents the different source type mechanisms and the AE hypocentre locations of events with amplitudes higher than 1000 μVolt, which represent the highest recorded amplitude events from specimen FB34. T-, S- and C-type events are illustrated in green, blue and red colours, respectively. Three different orthogonal projections are shown: i) normal to the specimen's axis (x-y plane), ii) parallel to the specimen's axis (y-z plane), iii) parallel to specimen's axis (x-z plane) and perpendicular to case ii.

AEs were grouped in four different time intervals corresponding to different loading stages. AEs hypocentre locations of the highest amplitude events indicated almost random distributions for increasing stresses up to the peak stress (Figure 1a, pre-failure stage). During this time interval, which lasted for more than 94 min, the number of the double couple (S-type) and collapse events was relatively the same, and slightly lower than that of the T-type events. AE activity concentrated on the mid-height of the Fb34 at a nucleation patch. Some of the AE activity nucleated from the place of the subsequent deformation band (Figure 1c), for stresses after the peak stress and before those of the failure (Figure 1b, pre-failure stage). Other AE events were spread along the mid-height section of the sample. This stage lasted for almost 16 min and was mainly dominated by collapse events, with S-type events being less than the half of the C-type events.

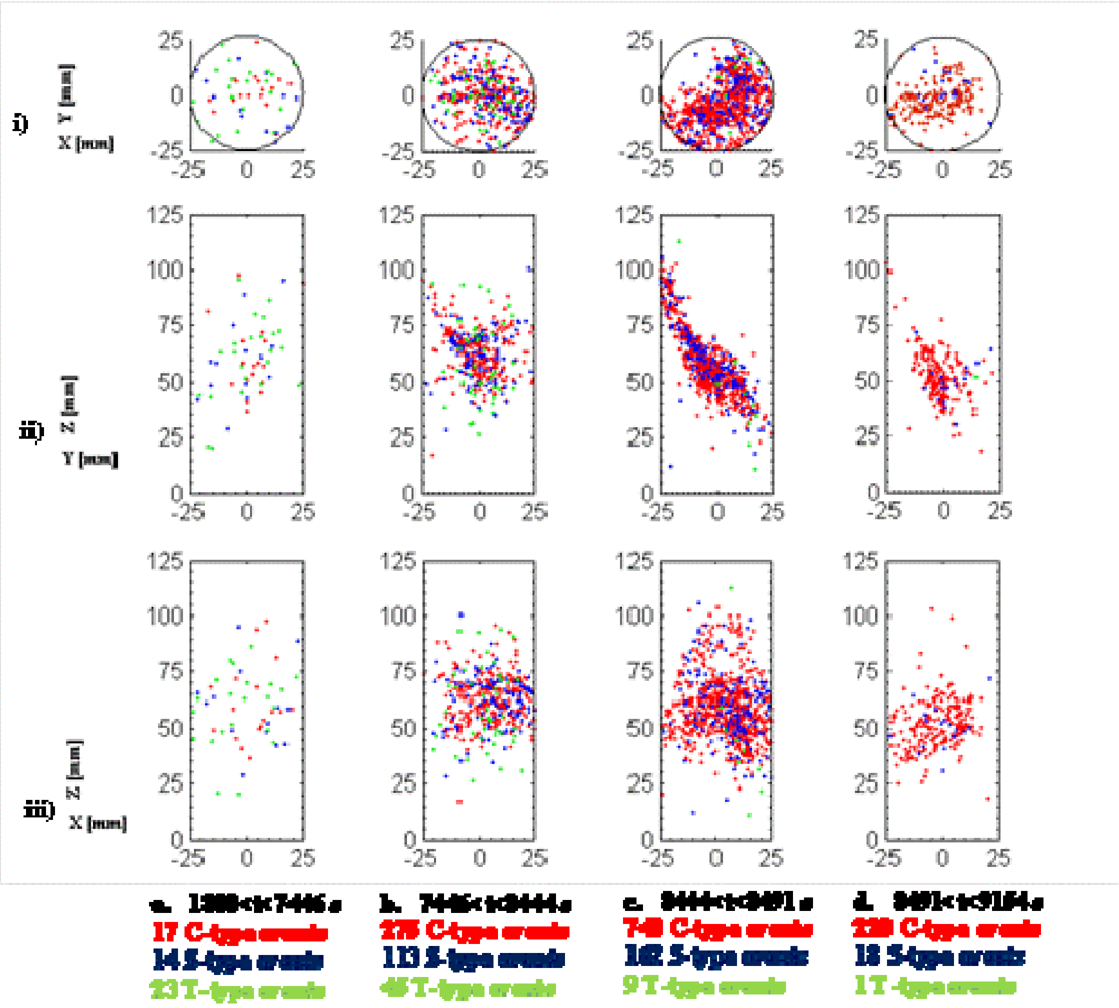

Figure 1: Source types and hypocentre locations from dry specimen Fb34. a) Pre-failure, stress hardening up to peak stress; b) Pre-failure, onset of axial stress softening after the peak stress; c) Failure, stress drop; d) Post-failure. AE events with amplitudes higher than 1000 µVolts are plotted.

During the actual failure (stress drop stage) all AEs were located in the fracture plane (Figure 1c, failure). This stage, which lasted for less than a minute, accumulated the greatest number of AE events with amplitudes higher than 1000µVolts. Collapse events were the great majority, while an increase in double couple events was also observed compared to the previous loading stages. In the post-failure stage, which lasted for almost 11 min (Figure 1d) mainly pore collapse events were monitored, while the number of double-couple events decreased drastically. The final fracture was halted 25 mm above the bottom of the specimen.

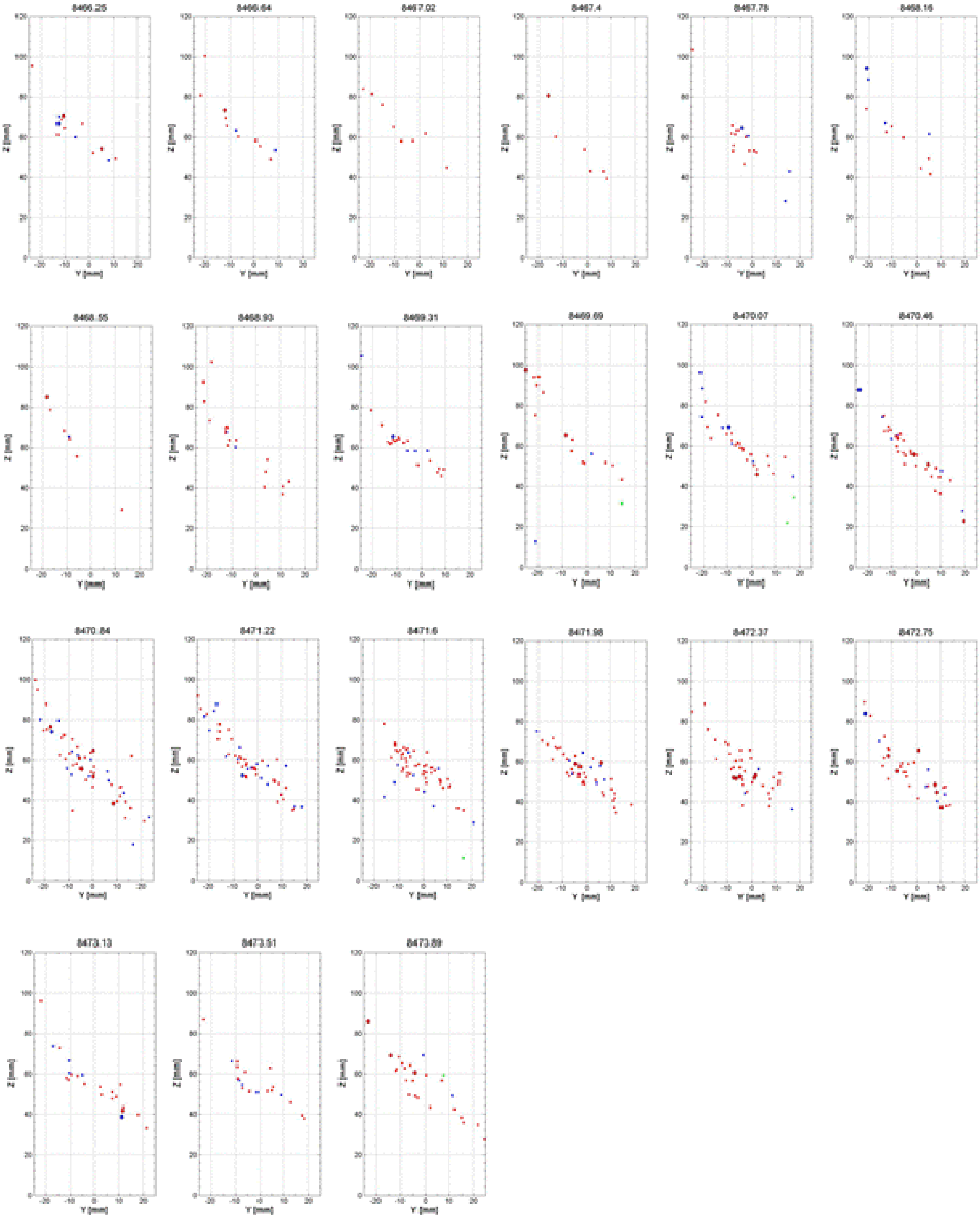

Figure 2: Source types and hypocentre locations from dry specimen Fb34 during the fault evolution. AE events with amplitude higher than 1000 μVolts are shown in circles, while AE events with amplitudes higher than 3162 μVolts are shown in diamonds. T-, S-, and C-type events are illustrated in green-blue and red colors.

Figure 2 presents in more details the source types of the AE activity during the failure (Figure 1c) projected to one of the parallel to the specimen's axis planes (y-z plane). T-, S-, and C-type events are shown in green, blue, and red colors, respectively. AE events with amplitudes higher than 1000 µVolts are represented by circles and AEs higher than 3162 µVolts are shown in diamonds. The fault propagation involved mainly by collapse events together with a relatively smaller, but no negligible, number of double couple events. The fault propagation was non-planar and evolved by the coalescence of crack clusters. Lower amplitude events clustered around higher amplitude events, which might be either S- or C-type events.

The bedding planes in specimen Fb35 were relatively stronger compared to those of specimen Fb34 and they could be visually seen both before and after the deformation of the specimen.

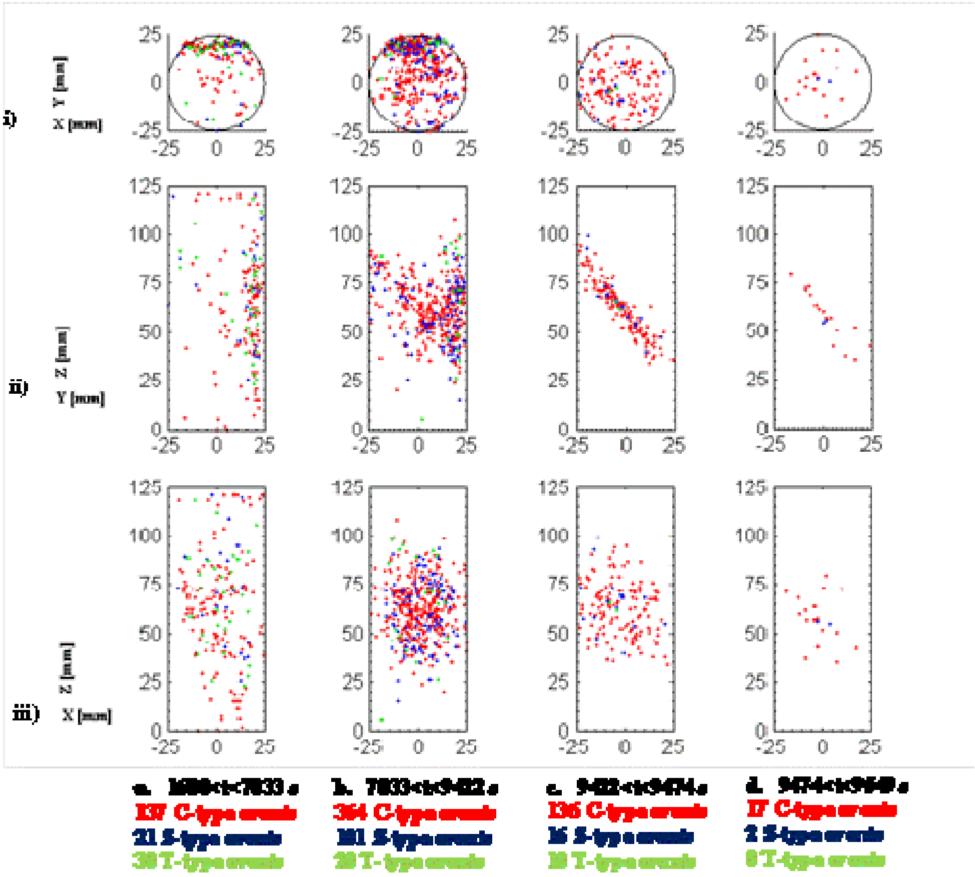

Figure 3: Source type and hypocentre locations from dry specimen Fb35. a) Pre-failure, stress hardening up to peak stress; b) Pre-failure, onset of axial stress softening after the peak stress; c) Failure, stress drop; d) Post-failure. AE events with amplitudes higher than 1000 µVolts are plotted.

Figure 3 presents the AE locations and the source type events from specimen Fb35 in vertical (i) and parallel (ii, iii) to the specimen's axis orthogonal projections. AE activity with amplitudes higher than 1000 μVolts is shown in four different time intervals, corresponding to different loading stages. During initial axial loading stage, most of the AE activity was concentrated on the vertical bedding plane (Figure 3a i-iii, pre-failure stage). The majority of AE events were collapse events, most of them located to the bedding plane, while the number of S- and T-type events was much smaller and comparable to that observed in specimen Fb34 for the same loading stage. After the peak-stress and before the failure, AE events were located in both the bedding plane and the consequent failure plane (Figure 3b). During this stage, which lasted for almost 40 min (longer than the equivalent of specimen Fb34), the visible bedding plane was continuously strained; parts of the bedding plane consisted the nucleation points from which the subsequent deformation band developed. During the stress drop, which lasted less than a minute and was smaller than that in specimen Fb34 (Figure 3c) mainly collapse events occurred along the fracture plane. The post-failure stage lasted slightly more than one minute and was also dominated by collapse events. The final fracture was halted 30 mm above the bottom of the specimen

1.4.2. Re-activation of the fracture through fluid injection into dry specimen

Specimens Fb34 and Fb35 were loaded close to the critical stress state at 20 μm displacement control rate. Specimen Fb34 was previously loaded under hydrostatic compression at 80 MPa confining pressure, therefore, its constant displacement loading stage was much longer in order to reach the critical stress state, compared to that of specimen Fb35, which was loaded for a smaller period (less than 30 seconds), since the latter was very close to the critical stress state. The position of the piston was then fixed (in both experiments). Specimens were allowed to relax for a period before the application of constant force and their in situ saturation.

During the in situ saturation stage of specimen Fb35, fluid was injected from the bottom port. Distilled water was pumped through the specimen by applying a constant inlet flow rate of 5 ml/min up to the point that the inlet pore pressure reached a value very closed to 5 MPa. During this stage, the piston was moving free to maintain a constant axial force. As soon as the displacement limit (300 μm) was exceeded, the displacement of the piston was held constant and an abrupt stress drop occurred. The specimen was creeping for a while. This specimen was fractured by applying a constant inlet flow rate.

Figure 4 shows the fluid injection stage on the dry specimen Fb35. Three different orthogonal projections are presented (similar to Figure 1,Figure 2). The coordinates of the AE events are rotated at +15° to better visualise the fault's geometry in the 2D projections (i, ii, iii).

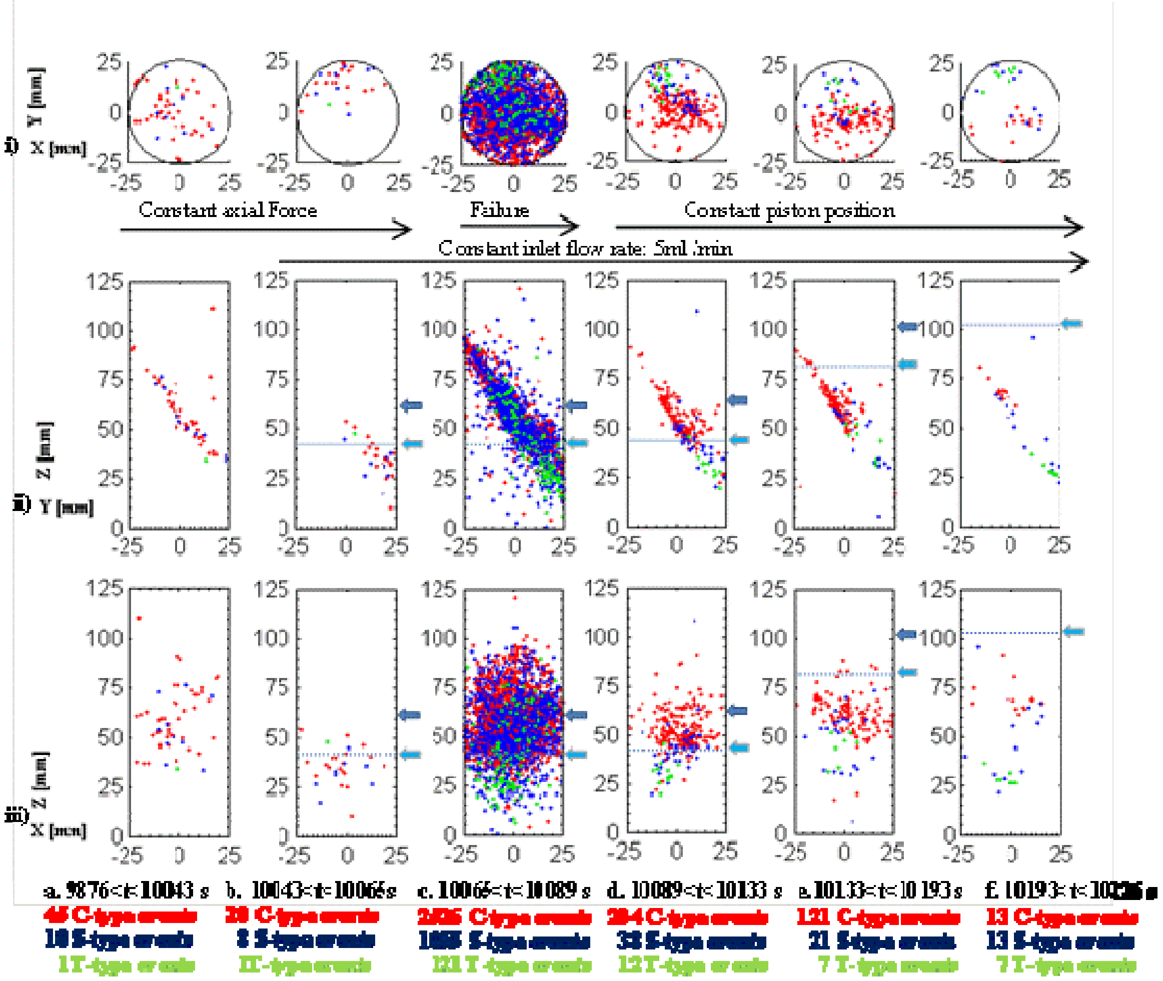

Figure 4: Source types and hypocentre locations during the distilled water injection into the dry specimen Fb35. a) Constant axial force stage; b) Constant axial force stage, onset of 5 ml/min inlet flow rate, change in velocities of sensors glued at z=+22.5 mm and z=+42.5 mm from the bottom of the specimen; c) Failure, 5 ml/min inlet flow rate; d) Constant displacement of piston stage, 5 ml/min inlet flow rate; e) Constant piston position stage, 5 ml/min inlet flow rate, change in velocities of sensors glued at z=+62.5 mm and z=+82.5 mm from the bottom of the specimen; f) Constant piston position stage, 5 ml/min inlet flow rate, change in velocities of sensors glued at z=+102.5 mm from the bottom of the specimen. AE events with amplitudes higher than 316 µVolts are plotted. T-, S-, and C-type events are shown in green, blue and red, respectively.

AEs with amplitudes higher than 316 µVolts are illustrated in six different time intervals, which correspond to either times of change in the horizontal velocities or times of particular loading conditions. The arrows in cyan colours represent the height of sensors for which horizontal velocities changed and the arrows in blue colours illustrate the height of sensors for which horizontal velocities remained constant during each of the presented time intervals. T-, S-, and C-type events are shown in green, blue and red colours, respectively.

When axial force was held constant (Figure 4a), fluid injection started by implying different inlet flow rates (i.e., 5 ml/min and 10 ml/min; for a total period of 79 seconds, which was included in the time interval of Figure 4a). The inlet pore pressure during this period was smaller than 0.65 MPa. During this stage, AE events were located on the fault's plane and had amplitudes much lower than 1000 µVolts. Most of them were collapse events.

During the in situ saturation of this specimen, the water front propagation had influenced the horizontal velocities of sensors glued at different heights (Figure 4b-f). The failure was dominated by collapse and double couple events, although the former were much more than the latter (Figure 4c). AE events were located along a fault plane, which was longer than the primary fault plane (see Figure 3b). The new fractures of this secondary re-activated fault (i.e., below the tip of the primary fault) were mainly T-type and S-type, while new fractures above the tip of the primary fault were mainly dominated by collapse and double couple events. During the creeping stages, mostly collapse events occurred along the fault plane (Figure 4d-f).

Figure 5 presents in more details the source types from AE events located along the re-activated fault plane during the failure stage. T-, S-, and C-type events are shown in green, blue and red colours, respectively. AE events with amplitudes higher than 316 µVolts, 1000 µVolts and 3162 µVolts are illustrated in small circles, big circles and diamonds, respectively. Cyan lines on the right of each image represent the water front level and blue ones stand for the potential water front level (similarly to arrows in Figure 4). Few AE events nucleated in places below the assumed water front level and progressively propagated along the fault plane. Collapse events expanded dominantly along the whole length of the fault. Higher amplitude events occurred during the subsequent stages (e.g. t=10077.1-10082.6 seconds, Figure 5). High amplitude S- and T-type events were mainly located at the tip of the primary 'locked' fault, which was re-activated and further evolved in this stage due to the fluid injection.

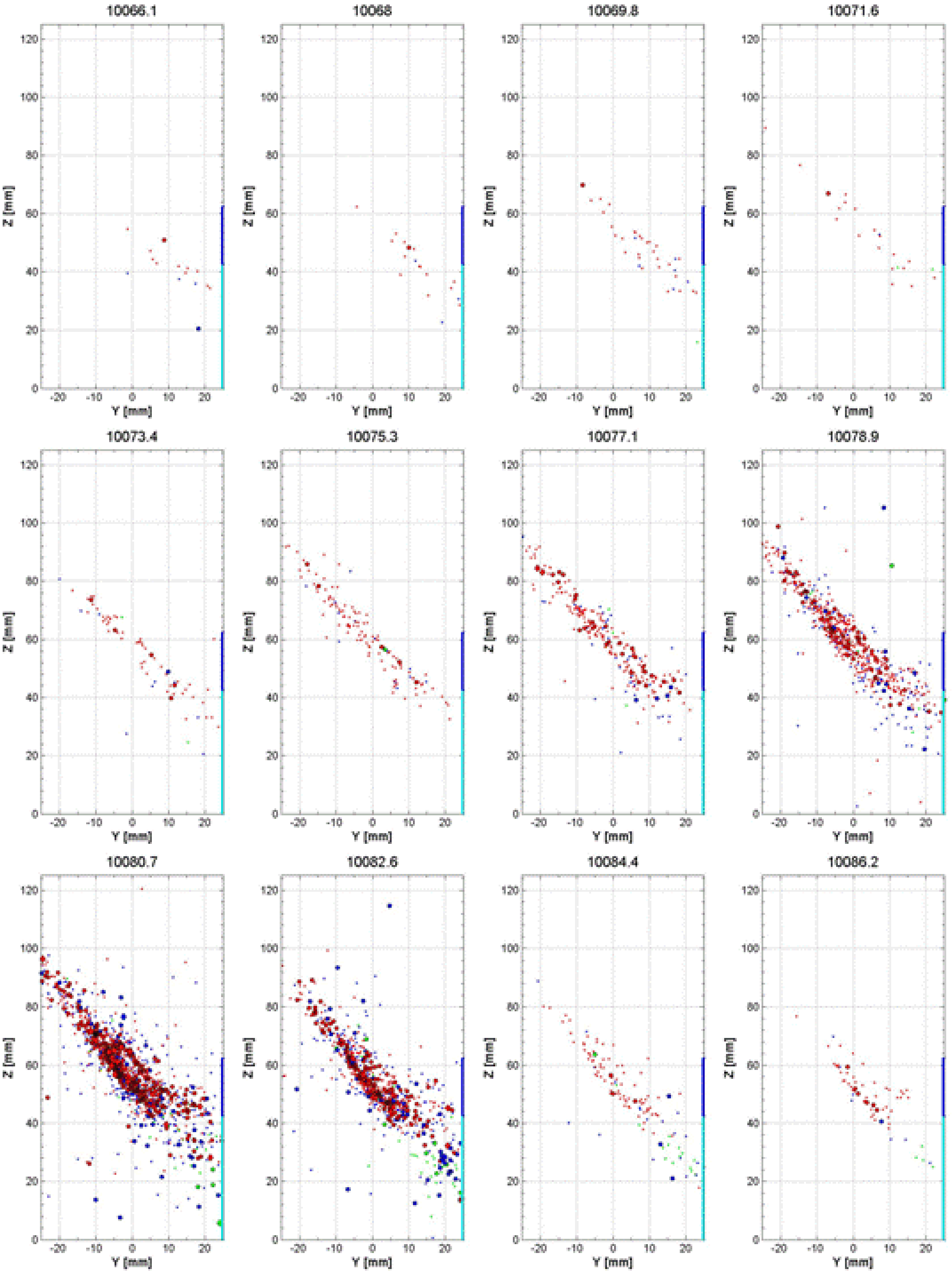

Figure 5: Source types and hypocentre locations during water injection in dry specimen Fb35. AE events with amplitudes higher than 316 μVolts are shown in small circles. AE events with amplitudes higher than 1000 μVolts are visualised in big circles, while AE events with amplitudes higher than 3162 μVolts are shown in diamonds. T-, S-, and C-type events are illustrated in green-blue and red colours.

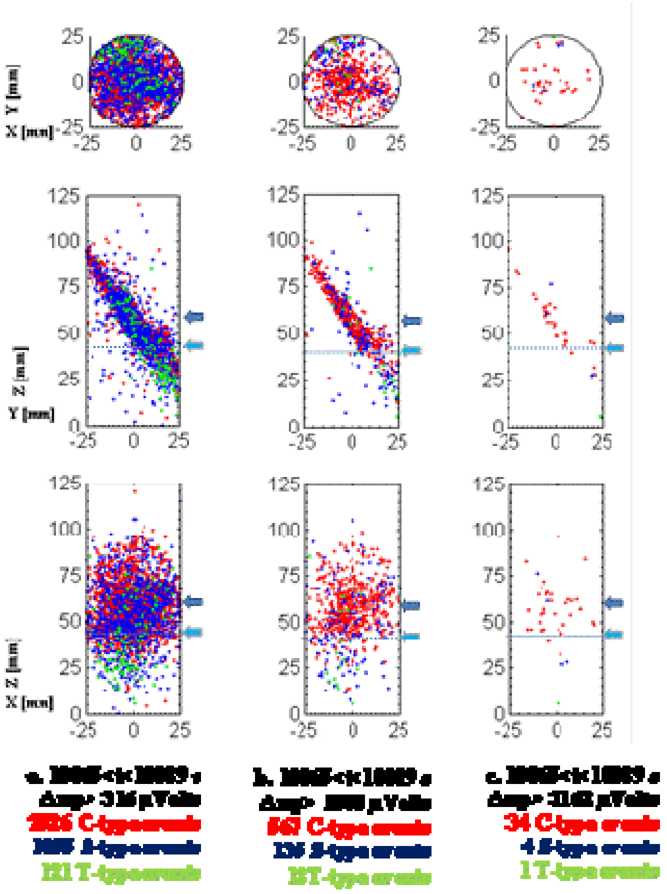

Figure 6: Specimen Fb35: source types and hypocentre locations during the failure of the re-activated fault. a) AEs with amplitude higher than 316 μVolts ; b) AEs with amplitude higher than 1000 μVolts ;c) AEs with amplitude higher than 3162 μVolts. T-, S-, and C-type events are shown in green, blue and red, respectively.

Figure 6summarizes in three orthogonal projections the source types of different AE events occurred during the fault re-activation due to fluid injection, grouped in events of different amplitudes (e.g., higher than 316, 1000, and 3162 μVolts). Collapse events had the greatest population of higher amplitudes compared to double couple or T-type events. Note that for the failure stage the number of the located collapse events with amplitudes between 316 and 1000 μVolts is 1959, with amplitudes higher than 1000 μVolts and lower than 3162 μVolts is 533, and with amplitudes higher than 3162 μVolts is 34. The number of the double couple events with amplitudes greater than 316 and lower than 1000 μVolts is 920, with amplitudes higher than 1000 μVolts and lower than 3162 μVolts is 131, and with amplitudes higher than 3162 μVolts is 4. Finally, 103 T-type located events had amplitudes between 316 and 1000 μVolts, 17 had amplitudes between 1000 and 3162 μVolts, and only 1 had amplitude higher than 3162 μVolts.

During the in situ saturation stage of specimen Fb34, distilled water was injected from the bottom port, by applying a constant inlet pore pressure equals to 5 MPa, until the re-activation of the pre-exiting natural fault. During this stage, the piston was moving free to maintain a constant axial force. As soon as the displacement limit (300 µm) was exceeded, the displacement of the piston was set constant and a sudden stress drop occurred. This specimen was fractured under a constant pore pressure.

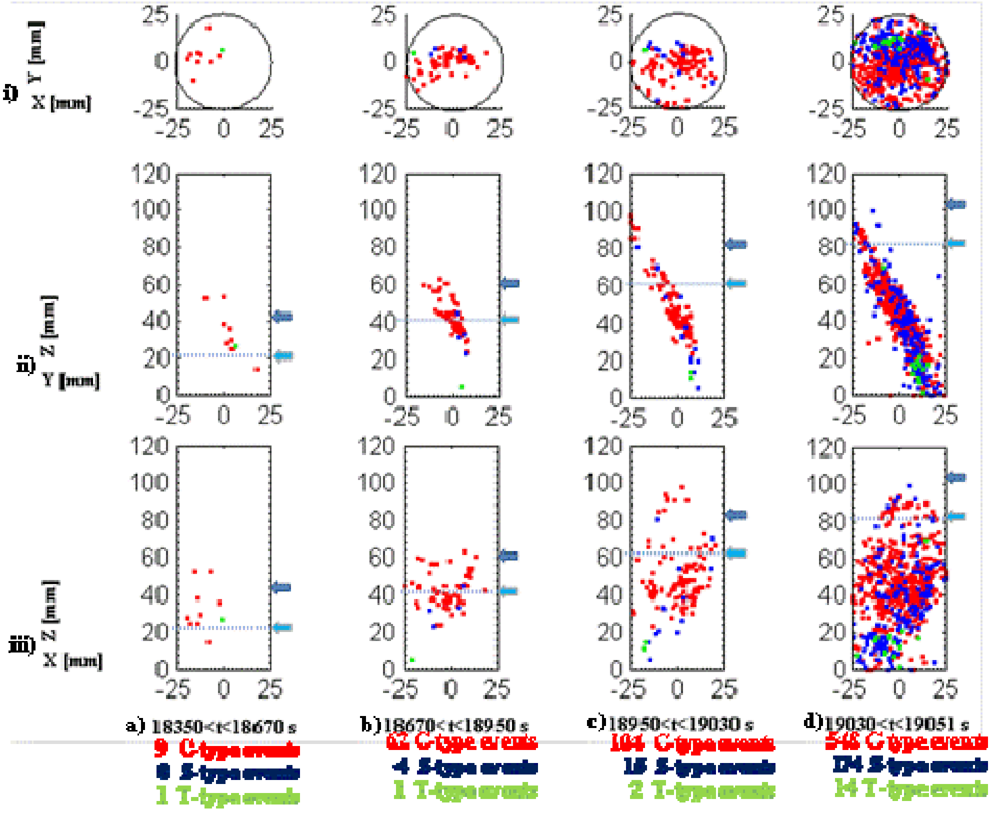

Figure 7: Source types and hypocentre locations during the distilled water injection into the dry specimen Fb34. a) Constant axial force stage, inlet pore pressure equals to 5 MPa, change in velocities of sensors glued at z=+22.5 mm; b) Constant axial force stage, inlet pore pressure equals to 5 MPa, change in velocities of sensors glued at z=+42.5 mm; c) Constant axial force stage, inlet pore pressure equals to 5 MPa, change in velocities of sensors glued at z=+62.5 mm; d) Constant axial force stage, inlet pore pressure equals to 5 MPa, change in velocities of sensors glued at z=+82.5 mm. AE events with amplitudes higher than 1000 µVolts are plotted. T-, S-, and C-type events are shown in green, blue and red, respectively.

Figure 7 presents the fluid injection stage from the dry specimen Fb34 (during the in situ saturation). Three different orthogonal projections are presented (i, ii, iii). AEs with amplitudes higher than 1000 µVolts are illustrated in four different time intervals, which correspond to times of change in the horizontal velocities. The colors of the arrows in the right of each projection have a similar meaning to that in Figure 4. T-, S-, and C-type events are shown in green, blue and red colors, respectively.

During the in situ saturation of the specimen, the horizontal velocities of sensors glued at different heights were affected by the water front propagation (see arrows in Figure 7). Induced seismicity was monitored also in places above the assumed water level, due to the migration of water along the fractures of the pre-existing 'locked' fault, which started being re-activated. The actual failure, which occurred within 21 seconds, was dominated by collapse and double couple events (the latter were much less than the former (Figure 7d)). AE events were located along a fault plane, which was longer than the primary fault plane (see Figure 1c, similar to Figure 3b). Note that the number of AE events of different source types during the failure stage is very similar to that in Figure 4.

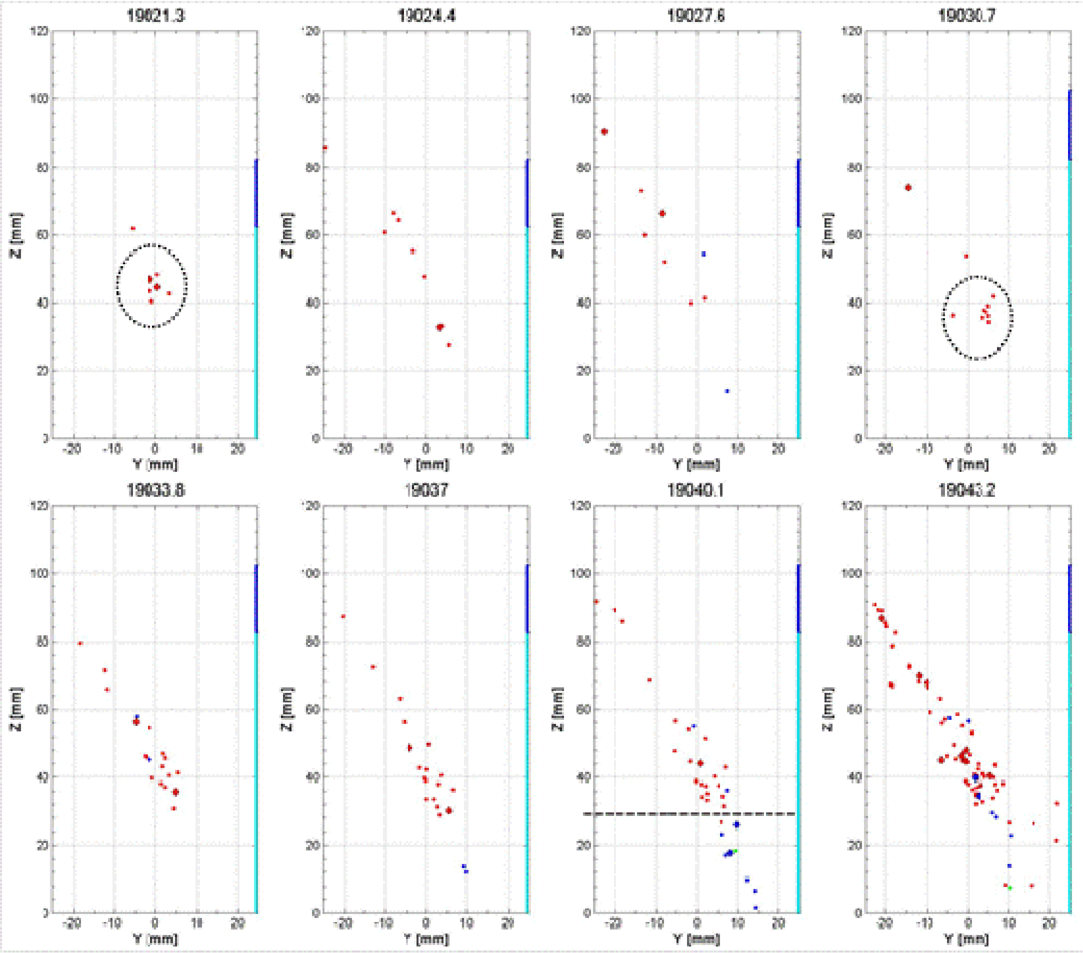

Figure 8: Source types and hypocentre locations from dry specimen Fb34 during water injection. AE events with amplitudes higher than 1000 µVolts are visualised in circles, while AE events with amplitudes higher than 3162 µVolts are shown in diamonds. T-, S-, and C-type events are illustrated in green-blue and red colours.

Figure 8 illustrates in more details the source types from AE events located along the re-activated fault plane slightly before and during the failure stage. T-, S-, and C-type events are shown in green, blue and red colours, respectively. AE events with amplitudes higher than 1000 µVolts and 3162 µVolts are shown in circles and diamonds, respectively. Cyan lines on the right of each image represent the water front level and blue ones the potential water front level (similarly to arrows in Figure 7). Dominantly collapse cracks nucleated along the existing fault. During the failure stage the tip of the pre-existing fault was highly stressed (Figure 8, in black circles). The new fractures at the bottom part of the re-activated fault were dominantly shear type cracks.

1.4.3. Re-activation of the fracture through fluid pressure pulse into saturated specimen

Specimen Fb34 was loaded twice more under triaxial compression, at 100 MPa and 120 MPa confining pressures and 25 MPa and 45 MPa inlet pore pressures, respectively. During these two stages, the Fb34 was fully saturated. The re-activation of the pre-existing fractures occurred in both cases under constant axial load (note that previously the specimen was loaded close to the critical stress state) due to the pore pressure gradient along the length of the specimen (equilibrium was not reached before the failure).

Figure 9 shows three orthogonal projections of the source types of AE events during the failure of the Fb34 (loaded under triaxial compression at 100 MPa confining pressure and 25 MPa inlet pore pressure). Events were grouped in different amplitude ranges (AEs with amplitudes higher than 316 µVolts, higher than 1000 µVolts and higher than 3162 µVolts). Collapse and double couple events mainly characterised the failure stage, with collapse events having a bigger population of higher amplitudes compared to the S-type events. Furthermore, the number of the located AE events in the Fb34 saturated specimen during this failure stage was smaller (Figure 9b) than that observed during the failure of the same specimen when being dry and water was injected into it for the first time (see Figure 7d).

Figure 10 illustrates the different source types during the actual failure stage (Figure 9) in more details (and smaller time intervals). AE events with amplitudes higher than 316 µVolt are shown in circles and those with amplitudes higher than 1000 µVolts are shown in diamonds. T-, S-, and C-type events are presented in green, blue, and red colours, respectively. Collapse events were mainly concentrated on the central part of the re-activated fault, while S- and T-type events were principally located at the tips of the re-activated fault.

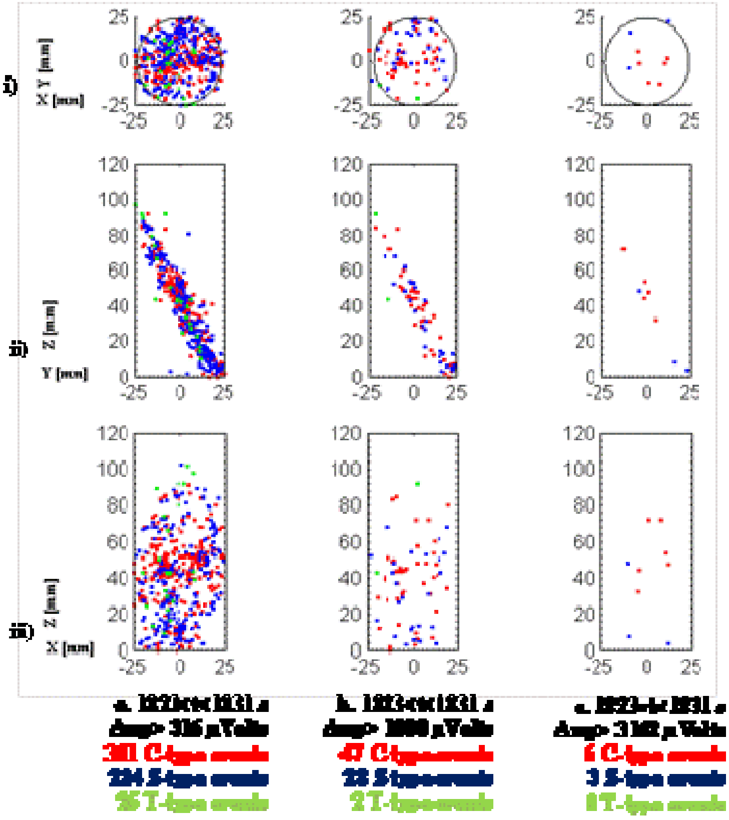

Figure 9: Saturated specimen Fb34: source types and hypocentre locations during the failure of the re-activated fault. a) AE events with amplitude higher than 316 µVolts ; b) AE events with amplitude higher than 1000 µVolts; c) AE events with amplitude higher than 3162 µVolts. T-, S-, and C-type events are shown in green, blue and red, respectively.

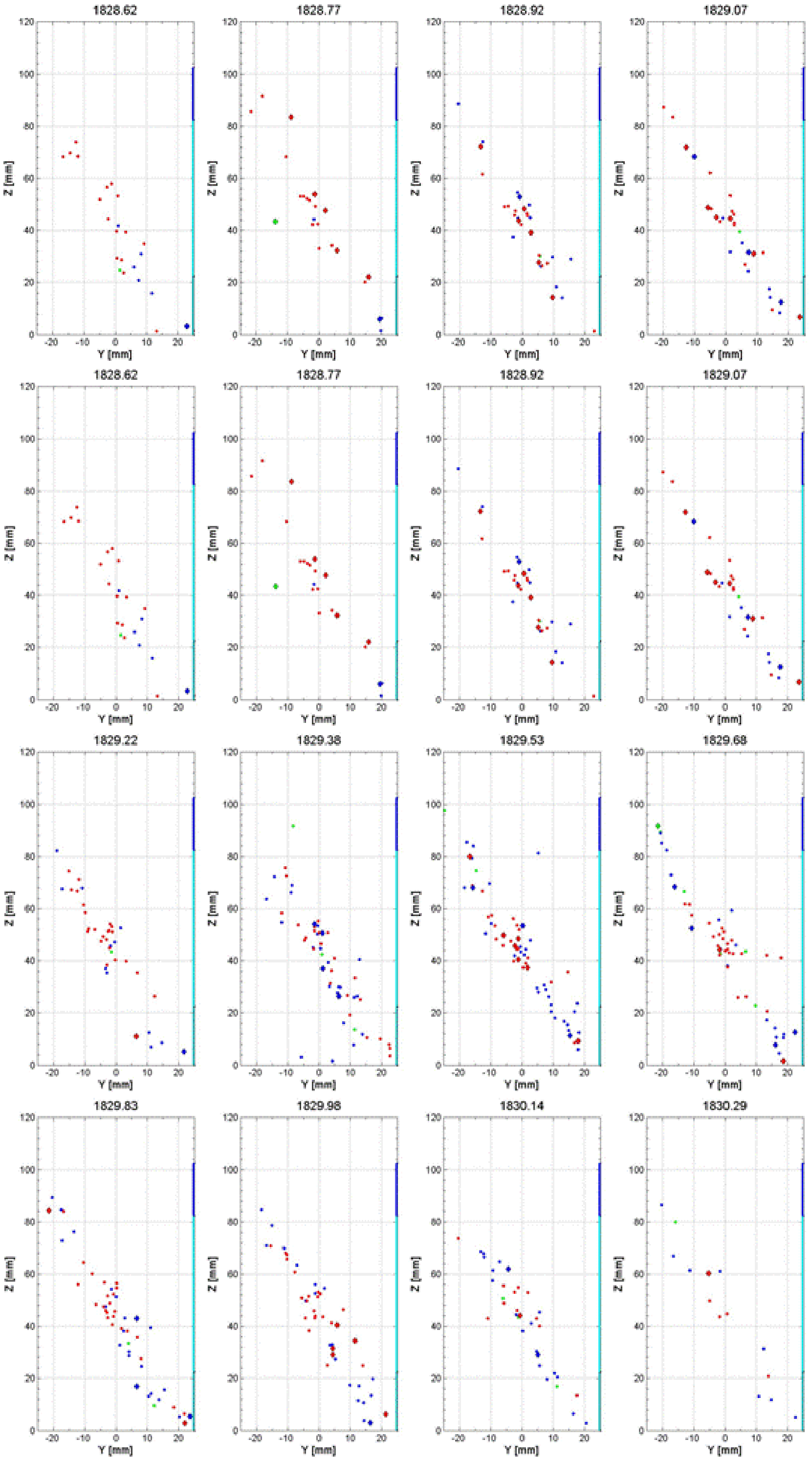

Figure 10: Source types and hypocentre locations from saturated specimen Fb34 during water injection. AE events with amplitudes higher than 316 µVolts are visualisedin circles, while AE events with amplitudes higher than 1000 µVolts are

shown in diamonds. T-, S-, and C-type events are illustrated in green-blue and red colours.

Figure 11 illustrates the different event types during the failure of the Fb34 (loaded under triaxial compression at 120 MPa confining pressure and 45 MPa inlet pore pressure), plotted in three planar projections (i, ii, iii) and grouped in three different amplitude ranges (a, b, c).

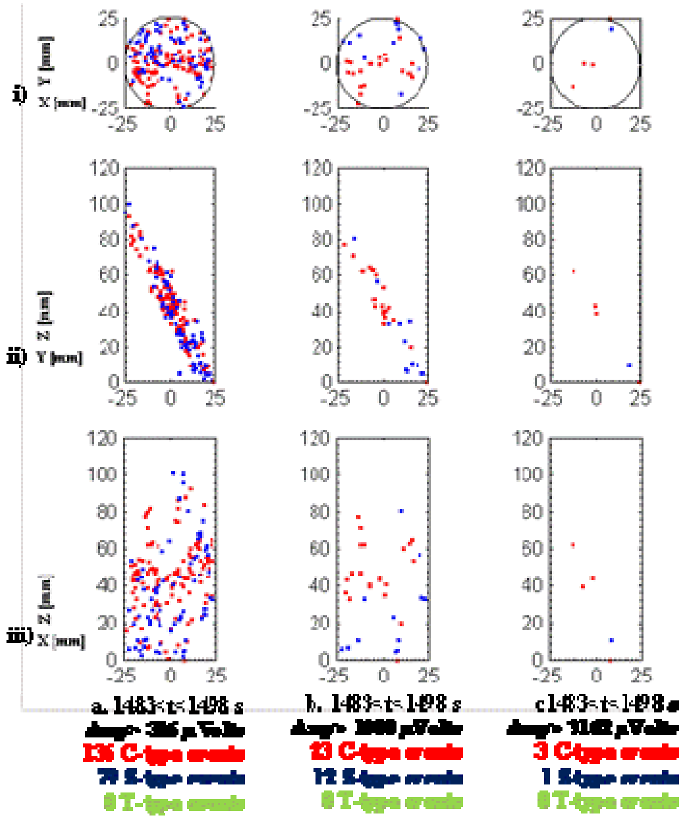

Figure 11: Saturated specimen Fb34: source types and hypocentre locations during the failure of the re-activated fault. a) AE events with amplitude higher than 316 µVolts ; b) AE events with amplitude higher than 1000 µVolts; c) AE events with amplitude higher than 3162 µVolts. T-, S-, and C-type events are shown in green, blue and red, respectively.

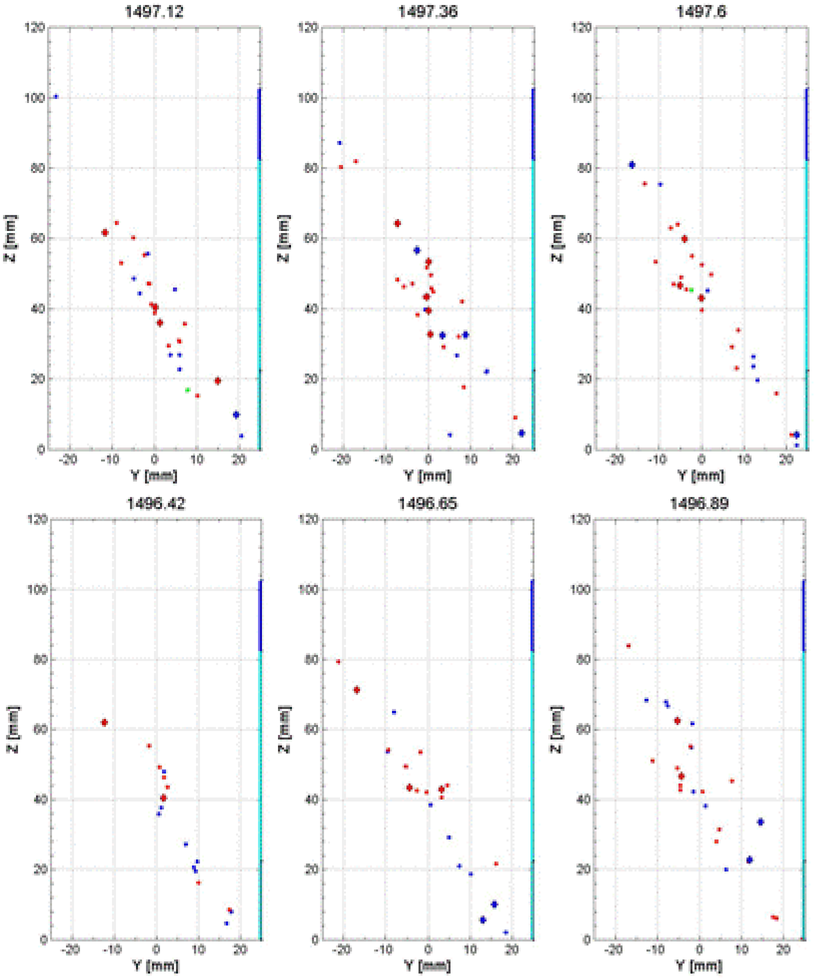

Figure 12: Source types and hypocentre locations from saturated specimen Fb34 during water injection. AE events with amplitudes higher than 316 µVolts are visualised in circles, while AE events with amplitudes higher than 1000 µVolts are shown in diamonds. T-, S-, and C-type events are illustrated in green-blue and red colours.

No T-type events were resolved during this stage. The failure was characterised dominantly by C-type events and a smaller number of S-type events. Note that the number of nucleated AE events was much smaller than in two previous re-activations of the fault (Figure 7 and Figure 9).

Figure 12illustrates in more details the evolution of the fault's re-activation. AE events with amplitudes higher than 316 µVolts, and 1000 µVolts are shown in circles and diamonds, respectively. T-, S-, and C-type events are represented in green, blue and red colours, respectively.

1.4.4. Re-activation of a pre-cut fracture through fluid pressure increase into saturated specimen

In this section, results from the saturated saw-cut specimen FL1 are presented. This specimen was loaded under triaxial compression 80 MPa confining pressure, and was fully saturated with distilled water before the application of the constant axial force. The initial inlet and outlet pore pressure was of 1MPa. Distilled water was pumped through the specimen (4 ml) by keeping a constant inlet flow rate of 0.1 ml/min.

Figure 13illustrates different source types in three orthogonal projections before, during and after the failure. Note that during these three stages the axial force was held constant (apart from the stress drop stage), because the displacement range of the piston was set to 1000 µm, which was much higher than the displacement of the fault.

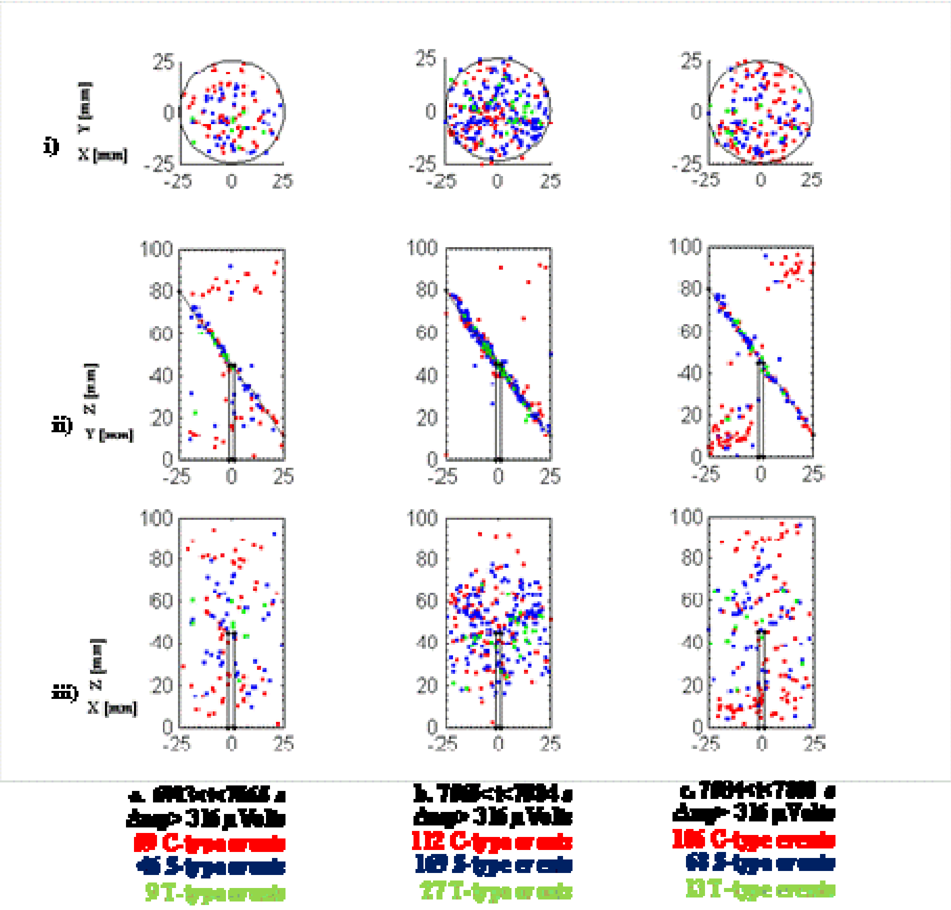

Figure 13: Source types and hypocentre locations from saturated specimen FL1 before (a), during (b) and after (c) the saw-cut plane re-activation due to increasing pore pressure. AE events with amplitude higher than 316 µVolts are shown in circles. T-, S-, and C-type events are illustrated in green-blue and red colours.

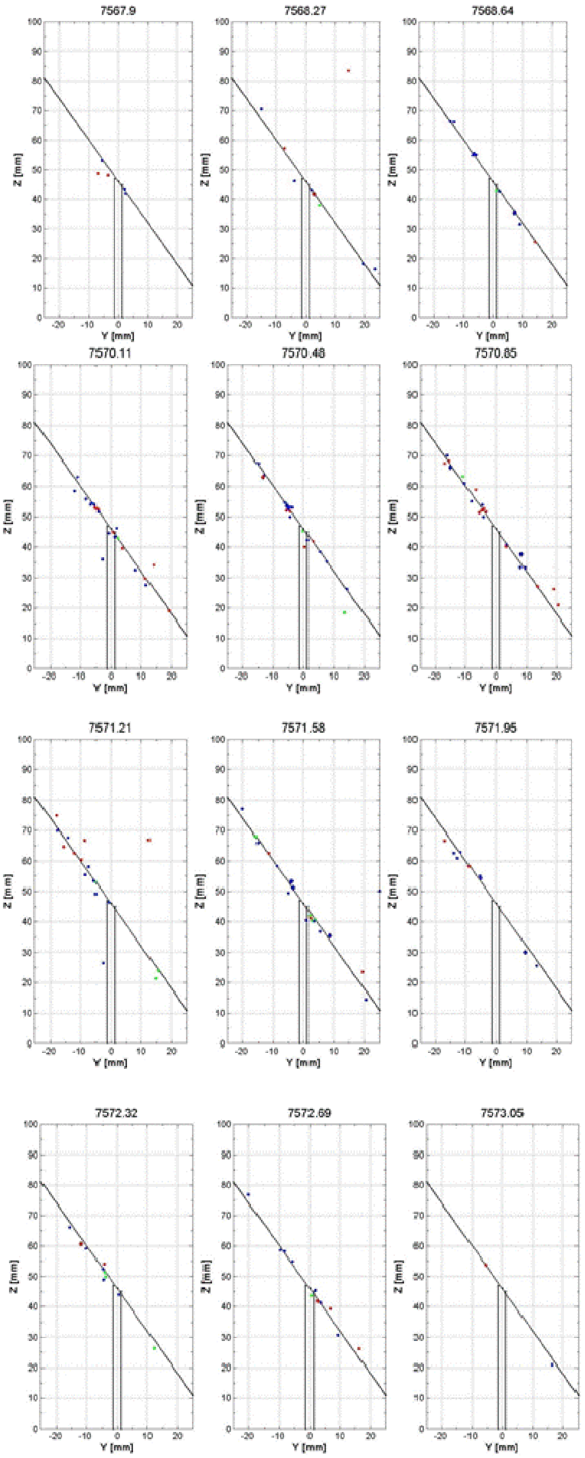

Figure 14: Source types and hypocentre locations from saturated specimen FL1 during the saw-cut plane re-activation. AE events with amplitude higher than 316 µVolts are shown in circles, while AE events with amplitudes higher than 1000 µVolts are shown in diamonds. T-, S-, and C-type events are illustrated in green-blue and red colours.

Saturated saw-cut specimen FL1, which was deformed under triaxial compression at 80 MPa, developed multiple deformation bands, while being loaded close to the critical stress state. Deformation bands were also recorded at the tips of the saw-cut plane. These bands were inclined in high angles towards the principal stress direction. When the axial stress was held constant, and before the failure (Figure 13a), AE events were mainly concentrated to the saw-cut plane and few collapse events nucleated also at the inclined deformation bands. During the failure (Figure 13b) the vast majority of AE events were located at the saw-cut plane. These events were dominantly double couple and collapse events. Note the that number of the former was bigger than that of the latter, while an non negligible number of T-type cracks also evolved along the fault plane. After the failure and while being still under constant axial stress (Figure 13c), AE events started being located in both the saw-cut plane and the pre-existing deformation bands. In this stage the number of S-type events decreased (in half). The number of the C- and T- events also diminished but in a smaller degree.

Figure 14illustrates the event types during the activation of the saw-cut plane (Figure 13b) in more details. All events are located along the saw-cut plane in different patches. Note, that the number of the located events is much higher compared to that of the saturated specimen Fb34 during the fault reactivation (section 1.4.3). This should be linked to the degree of roughness of the actual failure planes.

1.5. RESULTS

In this report, the 4D induced micro-seismicity from sandstone specimens (being deformed at the laboratory scale applying a constant axial force during the different injection scenarios), in terms of source types and the hypocentre locations, is presented. At the failure stage during the injection part the huge majority of the AE events was located along the pre-existing natural (Fb34, Fb35) or artificially created (FL1, saw-cut) fault planes. Increased fluid pressure decreased the effective stress state and leaded to fracturing and sliding along pre-existing faults.

The fractures during the failure stage of dry specimens (Fb34 and Fb35) were dominantly characterised by the highest amplitude events. The coalescence of C- and S-type cracks leaded to the actual fault formation and propagation. The fault plane was non-planar.

During fluid injection into dry specimens (Fb35 and Fb34, either by constant inlet flow rate or constant inlet pore pressure), fractures were re-activated possibly due to fluid migration along the pre-existing fault plane. In this stage, the re-activation was dominantly linked to collapse events. New fractures at the tip of the pre-existing fault were mainly S-type.

The re-activation of the fracture through fluid pressure perturbations into saturated specimen (Fb34) was characterised by fewer high amplitude events, which can be explained due to possibly smoother fracture surfaces related to the continuous re-activations of the fault planes. In this stage dominantly collapse and double couple events were monitored.

The first re-activation of a pre-cut surface through fluid pressure increase into saturated specimen (FI1) was initially characterised by the concentration of AE events in different patches along this surface. During the failure, S-type cracks dominantly evolved, while relatively higher number of C-type cracks developed before and after the re-activation. Along the saw-cut plane, the number of AE events with the highest amplitudes was bigger than that observed along the second and third re-activation of a naturally created fault due to fluid pressure perturbations in saturated specimens (Fb34). This might be linked to possibly smoother surfaces of the continuously re-activated natural fault compared to those of the saw-cut plane when it was re-activated for the first time. However, the number of the highest amplitude events along the saw-cut plane is much smaller than that observed during the first re-activation of a fault in a dry specimen due to fluid injection.

1.6. PERSPECTIVES, FOLLOWED-UP EVENTS AND PUBLICATIONS

The results from experiments presented in this final report from Task 4.1 were focusing on the role of pore pressure change on the failure of sandstone due to different fluid injection scenarios (either by keeping a constant pressure control or flow rate) and complemented results presented in Stanchits et al., [2011], where fracturing of the same rock induced by fluid injection was studied. Specimens from the latter study were either solid or with a central borehole. The originality in the present study lies in the re-activation of the naturally created fault by consecutive ‘locking’ of the pre-existing fault either on a dry or saturated specimen’s environment, and the introduction of the saw-cut plane and the re-activation of the saw-cut fault. Further experiments on saw-cut samples will be presented on the report from Task 4.3.

The results from this report have already been presented in the two last WP4 work progress internal meetings (26th May 2011, BRGM, Paris, France and 4th November 2011, ETH, Zurich, Switzerland), as well as in the 9thEuroconference on Rock Physics and Geomechanics (17-21 October 2011, Trondheim, Norway).

The manuscript of an article entitled: ‘Monitoring induced seismicity due to fluid injections at the laboratory scale’ is under preparation. This article is going to be submitted to the International Journal of Rock Mechanics deriving from the Special Volume from the 9thEuroconference.

Further inter group collaboration between GFZ and ETHZ is planned for the calculation of b-values from the AEs monitored during the injection phases.

Furthermore, more experiments are planned on samples provided to GFZ by Iceland GeoSurvey, directly from the Reykjanes geothermal site in Iceland (see section 2). These experiments are planned to take place in the spring of 2012.

1.7. REFERENCES

Ellenberg , J., Falk, F, Grumbt, E., Lützner, H., Ludwig, O., 1976. Sedimentation des höherenUnterperms der FlechtingerScholle. Z. Geol. Wiss. 4, 705-737 (in German).

Leonard, M., Kennett, B.L.N., 1999.Multi-component autoregressive techniques for analysis of the seismograms.Phys. Earth Planet.Inter. 113 (1-4), 247.

Lockner, D.A., Byerlee, J.D., Kuksenko, V., Pomomarev, A., Sidorin, A., 1991. Quasi-static fault growth and shear fracture energy in granite. Nature 350, 39-42.

Lockner, D.A., Byerlee, J.D., Kuksenko, V., Pomomarev, A., Sidorin, A., 1992. Observations of quasistatic fault growth from acoustic emissions. In: Evans, B., Wong, T.-F. (Eds.), Fault Mechanics and Transport Properties of Rocks. Academic Press, London, pp. 3-31.

Nelder, J., Mead, R., 1965. A simplex method for function minimisation.Comput. J. 7, 308-312.

Stanchits, S., Vinciguerra, S., Dresen G., 2006. Ultrasonic velocities, acoustic emission characteristics and crack damage of basalt and granite. Pure and Applied Geophysics 163 (5-6), 975-994. Doi:10.1007/s00024-006-0059-5.

Stanchits, S., Fortin, J, Gueguen, Y., Dresen, G., 2009. Initiation and propagation of compaction bands in dry and wet bentheim sandstone. Pure and applied Geophysics 166, 843-868. Doi: 10.10007/BF00876395.

Stanchits, S., Mayr, S., Shapiro, S., Dresen, G., 2011. Fracturing of porous rock induced by fluid injection.Tectonophysics, 503, 129-145.

Zang, A.,Wagner, F.C., Dresen, G., 1996. Acoustic emission, microstructure, and damage model of dry and wet sandstone stresses to failure. J. Geophys. Res. 101 (8), 17507-17521.

Zang, A., Wagner, F.C:,Stanchits, S., Dresen, G., Andresen, R., Haidekker, M.A., 1998. Source analysis of acoustic emissions in Aue granite cores under symmetric and asymmetric compressive loads. Geophys. J. Int. 135, 1113-1130.

2. Core Samples for laboratory experiments

2.1. PREAMBLE

The role of ÍSOR in Task 4.1 involves collection and delivery of core sample material for laboratory tests performed by GFZ (see section 1). This section gives details on the code samples taken from Icelandic geothermal reservoirs.

2.2. CORE SAMPLES

The Reykjanes high temperature field is located on the SW tip of the Reykjanes peninsula where the Reykjanes ridge comes on shore in Iceland. It is an active area with recent volcanism and rifting. Location of the wells which the samples originate from is shown on Figure 15.

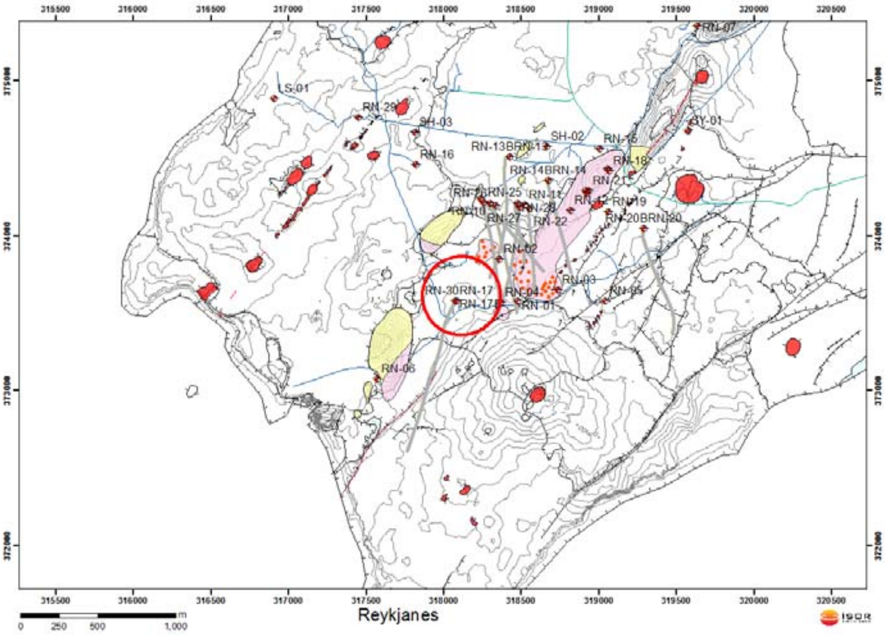
315500
316000
316500
317000
317500
318000
318500
319000
319500
320000
320500
375000
374000
373000
372000
RN-07
LS-01
RN-29
SH-03
SH-02
RN-15
GY-01
RN-13BRN-13
RN-16
RN-18
RN-14BRN-14
RN-21
RN-25
RN-11
RN-12
RN-19
RN-10
RN-28
RN-27
RN-22
RN-20BRN-20
RN-02
RN-03
RN-30RN-17
RN-17B
RN-04
RN-01
RN-05
RN-06
Reykjanes
0
250
500
1,000
m
ÍSOR

Figure 15 : The Reykjanes geothermal field. The location of the wells is marked with red circle. Well RN-17B is vertical and the track of well RN-30 is shown with a gray line. Red areas show postglacial eruption sites and yellow and pink denote areas of thermal alteration.

During drilling of wells no RN-17B and RN-30 ISOR performed coring at two depth intervals. RN-17B was originally thought to be the first part of a deep IDDP well in Iceland and the coring was supported by ICDP. The first core in RN-17b was taken close to 2500m depth. It consisted of typical high temperature altered hyaloclastite rock. The second core was collected from the newly drilled well RN-30 close to 2800m within a typical dolerite dyke that are abundant in the lower parts of the geothermal fields.

Both cores are representative samples for the dominant rock types in the reservoir part of the Icelandic high temperature systems and within the volume of induced seismicity. Hence these samples are very well suited for laboratory test of real reservoir rocks. Samples from both cores were sent for analysis to the rock physics lab of GFZ-Potsdam for detailed measurements of various physical parameters, especially properties related to deformation under hydrostatic and deviatoric compression or constant loading conditions in the laboratory. The measurements include the effective stress, the confining pressures, the axial and radial deformations, the pore pressures and the permeability (depending on the fluid injection conditions) during the experiments.

3. Structural heterogeneities compartmenting sedimentary reservoirs

3.1. PREAMBLE

The role of TNO in Task 4.1 aims at studying the potential effect of structural heterogeneity and reservoir compartmentalization on fault stability and induced seismicity in sedimentary reservoirs.

3.2. INTRODUCTION

Worldwide, numerous large magnitude events (LME's) have been associated with the production of gas from sedimentary reservoirs. Examples are the seismic events up to a magnitude of M=4.2 which occurred near the Lacq Field in southern France (Feigner and Gross, 1991) and the numerous seismic events in the Northern Netherlands, up to a magnitude of M=3.5 (Van Eck, 2006, Muntendam, 2008). The geomechanical processes and causes of induced seismicity associated with gas extraction have been extensively studied, with special focus on the role of poro-elastic effects during gas production and the role of the geometry of the reservoir and the fault structures. Numerical studies have shown that sealing fault structures and reservoir compartmentalization promote differential pore pressure evolution and differential compaction of the sedimentary reservoir rocks which can have a large effect on fault stability during gas production (Mulders, 2003, Muntendam, 2008). Insights gained from these studies performed for the oil & gas industry can be particularly relevant for understanding the mechanical processes during geothermal operations in sedimentary low permeability/high temperature reservoirs.

Here, induced seismicity and fault reactivation during gas production and occasional fluid injection in depleted gas reservoirs is used as an analogue for EGS in sedimentary reservoirs. One of the important similarities of EGS operations in sedimentary reservoirs and gas production from sedimentary reservoirs is the pore pressure change within the sedimentary matrix rocks. As opposed to EGS in impermeable crystalline rocks, pore pressure changes will not be restricted to the fracture network, but will extend into the matrix rocks between the fractures. Poro-elastic effects in the matrix rocks will lead to changes in effective stresses and strains in the matrix rocks and will induce additional stresses on (sealing) faults which are intersecting and bounding the reservoir rocks. Differential compaction of the reservoir rocks in case of gas production and differential expansion of the reservoir matrix rocks during water injection in EGS operations can have an impact on fault stability and seismic risk.

The differences between gas production and EGS operations are also evident. Enhanced geothermal systems will predominantly target for deep high temperature - low permeability (rather tight) reservoirs and a hybrid flow through both the fracture network and the low permeable matrix will occur. Gas production from the fields in the

Northern Netherlands predominantly takes place in permeable reservoir sandstones, with a negligible contribution of flow through induced fractures or existing fracture networks. Pore pressure distributions, gradients around producing wells and the area affected by the pore pressure changes will be different for EGS and gas production, due to the differences in diffusivity of the gas and water and the well scheme used for field development. Finally, pore pressures in the gas reservoir during gas or water injection into the depleted gas reservoirs will generally not exceed the original pore pressure in the reservoir, whereas during stimulation of the fracture network in EGS pore pressures will exceed the original reservoir pressures.

Aim of the present study is to assess the potential effect of structural heterogeneity and reservoir compartmentalization on fault stability and induced seismicity in EGS in sedimentary reservoirs. The effects of pore pressure changes in the rock matrix and the role of compartmentalization on fault stability are investigated for a field case of gas production from a sedimentary reservoir in the Northern Netherlands. Next, general insights on the impact of reservoir compartmentalization on fault stability and induced seismic hazard for EGS in sedimentary reservoirs are obtained from preliminary calculations, using a numerical model of water injection in a sedimentary reservoir, which is compartmentalized by a sealing fault. At present no data on EGS in compartmentalized reservoirs are available.

3.3. IMPACT OF PORO-ELASTIC STRESS CHANGES AND RESERVOIR COMPARTMENTALIZATION ON FAULT STABILITY

3.3.1. Poro-elastic effects of depletion and injection

Figure 16 shows shear and normal tractions on a faultplane with dip α in a horizontal reservoir of infinite horizontal extension. Due to the decrease in pore pressure during depletion of the reservoir the effective vertical stress $S_{V'}$ increases with a*ΔP (ΔP is the pore pressure change and a is the Biot constant; no stress arching assumed). A decrease in pore pressures results in an increase of the horizontal stresses, but the magnitude of horizontal stress change is smaller than ΔP. The magnitude of horizontal stress change depends on the depletion constant γ of the reservoir, which in the sedimentary reservoirs in The Netherlands generally varies between $\gamma=0.4$ and $\gamma=0.8$. In an extensional tectonic setting, such as encountered in the Netherlands, due to the differential increase of effective vertical and horizontal stresses during depletion, differential stresses in the reservoir rocks tend to grow (i.e. the Mohr circle for stress increases, see Figure 16). The opposite holds for injection: effective stresses and differential stresses in the reservoir rocks decrease during injection. Whether or not the stress development in the reservoir will cause fault reactivation depends on the inclination (i.e.tangent) of the stress path (see Figure 16, lower graphs).

Also shown (Figure 17) is the effect of water injection into a fracture in an impermeable rock mass. In this case, due to the pore pressure increase during injection into the fracture, the Mohr stress circle shifts towards the left. Injection into a fracture network in an impermeable rock mass will always lead to less stable stress conditions (critical stress path). The latter mechanism is regarded to be the dominant mechanism of fracture reactivation in EGS in non-sedimentary, low permeability fractured reservoirs.

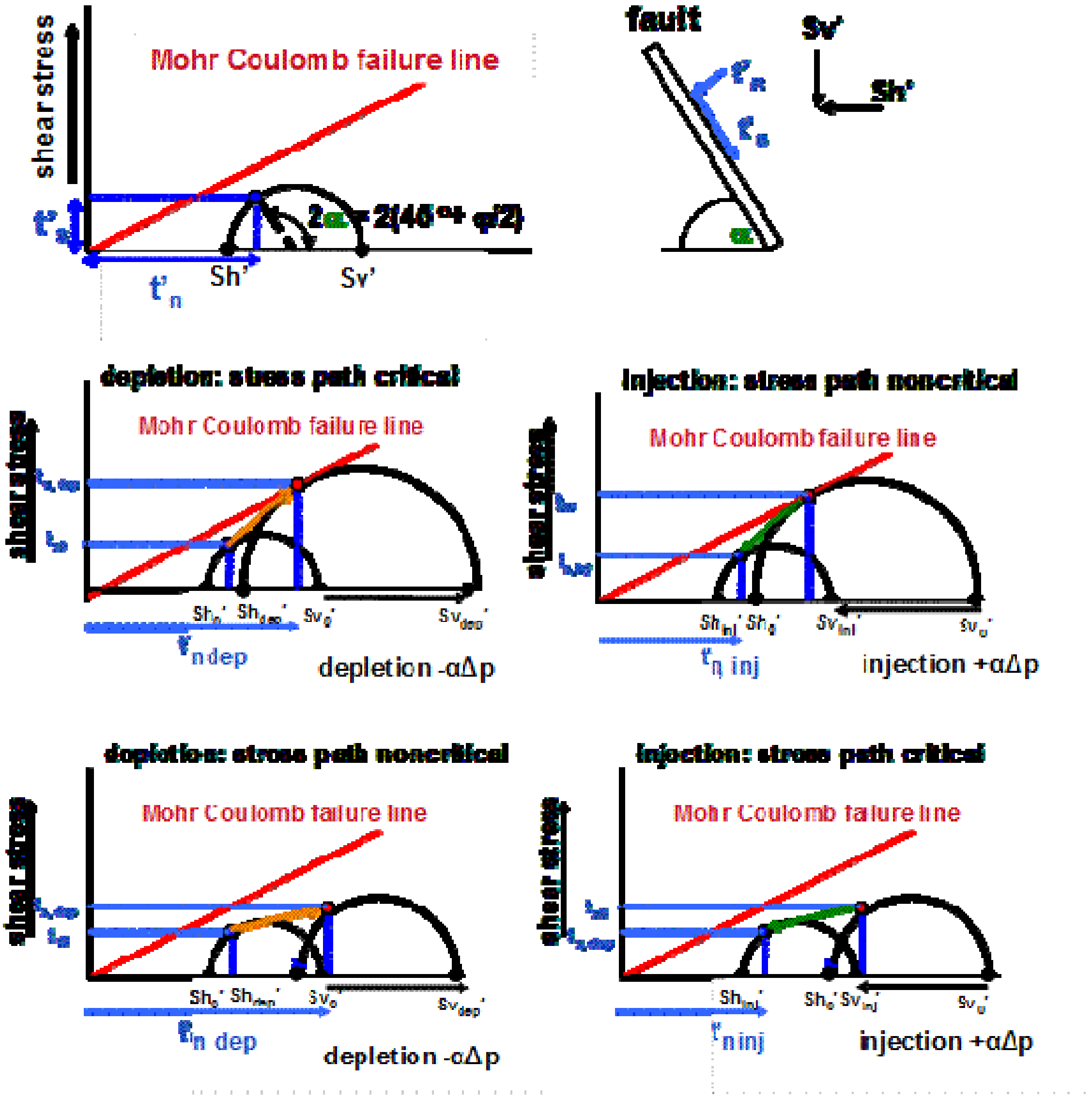
shear stress
Mohr Coulomb failure line
t'ₛ
t'ₙ
Sh'
Sv'
2α = 2(45° + φ/2)
fault
t'ₙ
tₛ
α
Sv'
Sh'
depletion: stress path critical
Mohr Coulomb failure line
shear stress
tₛ,dep
tₛ₀
Sh₀'
Sh_dep'
Sv₀'
Sv_dep'
t'ₙ dep
depletion -αΔp
injection: stress path noncritical
Mohr Coulomb failure line
shear stress
tₛ₀
tₛ,inj
Sh_inj'
Sh₀'
Sv_inj'
Sv₀'
t'ₙ inj
injection +αΔp
depletion: stress path noncritical
Mohr Coulomb failure line
shear stress
tₛ,dep
tₛ₀
Sh₀'
Sh_dep'
Sv₀'
Sv_dep'
t'ₙ dep
depletion -αΔp
injection: stress path critical
Mohr Coulomb failure line
shear stress
tₛ₀
tₛ,dep
Sh_inj'
Sh₀'
Sv_inj'
Sv₀'
t'ₙ inj
injection +αΔp

Figure 16 : Stress paths on a critically oriented fault plane during reservoir depletion (left) and injection into a reservoir (right). Initial tectonic setting is extensional ($S_V>S_{Hmax}>S_{hmin}$). Upper figures show horizontal ($S_{h'}$) and vertical effective stress ($S_{V'}$), shear (t_s) and normal tractions (t'_n) on a critically oriented faultplane with dip α and the related Mohr circle for stress and Mohr failure envelope (φ is friction coefficient of the fault). Middle graph left shows stress path on the faultplane during depletion, which is critical (converging on the MC-line). Middle graph right shows stress path on the fault

plane during injection which is non-critical (diverging from the MC-line). Lower graph left shows stress path on the faultplane during depletion (non-critical). Lower graph right shows stress path on the faultplane during injection (critical). Subscript 0 means initial stress, subscripts dep and inj mean stresses after depletion resp. injection.

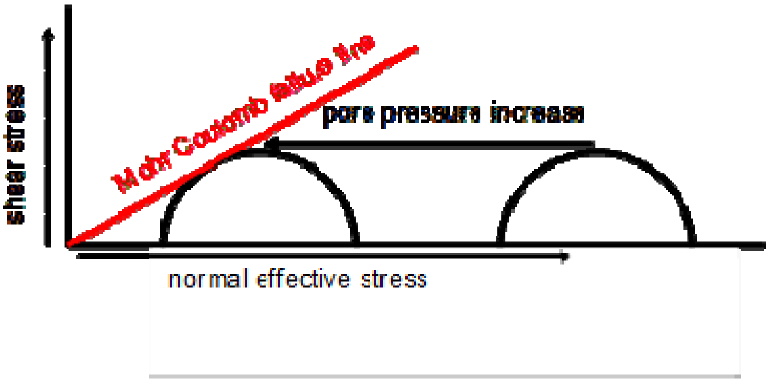

Figure 17 : Impact of injection of water into an open fracture / open fault in an impermeable or low permeable rock mass. Due to the pore pressure increase the Mohr circle shifts towards the left and normal effective stresses on the fracture decrease, resulting in potential fracture/fault reactivation. This is regarded the dominant mechanism for fracture reactivation in EGS in non-sedimentary, low permeability fractured reservoirs.

3.3.2. Geometrical effects of depletion of and injection into a sedimentary reservoir

Next to the poro-elastic effects, both the geometry of the reservoir and the strength and structure of the faults (offset, orientation, dip, strength) play an important role in fault reactivation and induced seismicity (Mulders, 2003). Figure 18 shows two schematic examples of the impact of reservoir geometry and compartmentalization on potential reactivation of reservoir faults in an extensional tectonic setting. Due to the decrease (or increase) in pore pressure compaction of the reservoir rocks takes place. If the reservoir is bounded or intersected by a sealing fault, compaction (or decompaction) of the reservoir rocks will lead to differential movements and an increase of shear stresses on the fault plane. Mulders (2003) showed this effect is largest if reservoir compartmentalization is present and reservoir rocks on both sides of the fault are partially juxtaposed, or if a small offset between the reservoir blocks exists. Depending on factors such as the amount of pore pressure change and (de)compaction, dip and orientation of the fault related to the stress regime and the amount of offset along the fault, differential (de)compaction can cause fault reactivation.

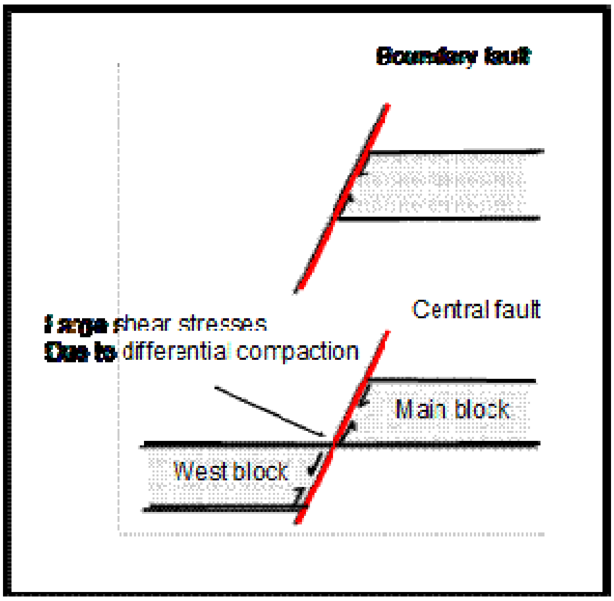

Figure 18 : Geometrical effects on differential compaction, fault shear tractions and the potential of fault reactivation.

Numerical modelling shows that both poro-elastic effects and reservoir geometry play an important role in the fault reactivation potential and induced seismicity during gas production in the northern parts of the Netherlands. An example of induced seismicity during gas production, which can be related to reservoir compartmentalization and differential compaction is presented below.

3.4. FIELD CASE: INDUCED SEISMICITY CAUSED BY GAS PRODUCTION FROM A COMPARTMENTALIZED RESERVOIR IN THE NORTHERN NETHERLAND

In the Northern parts of the Netherlands gas is produced from sedimentary (mainly sandstone) reservoirs at approximately 2 to 3 km depth. The exploitation of these gas fields has induced numerous small earthquakes with magnitudes up to M=3.5. For a number of these gasfields, taking into account the depletion history of the reservoir, the timing and location of fault reactivation and induced seismicity can be reproduced using geomechanical numerical modelling. For the field case presented here, the mechanism of fault reactivation during gas production in a small Rotliegend sandstone reservoir is analysed. The case shows that reservoir compartmentalization and differential compaction due to pore pressure changes plays an important role in the reactivation of the faults and induced seismicity.

In Figure 19 a schematic geology of the gas reservoir is shown, including the hypocenters of the seismic events which occurred during depletion of the reservoir. All seismic events have been localized on the tip of a central fault plane intersecting the reservoir. This fault is (partially) sealing and divides the reservoir into two main compartments. The (normal) offset of the south western reservoir block varies along the strike of the fault. Table 1 summarizes the main parameters of the reservoir and the depletion phase.

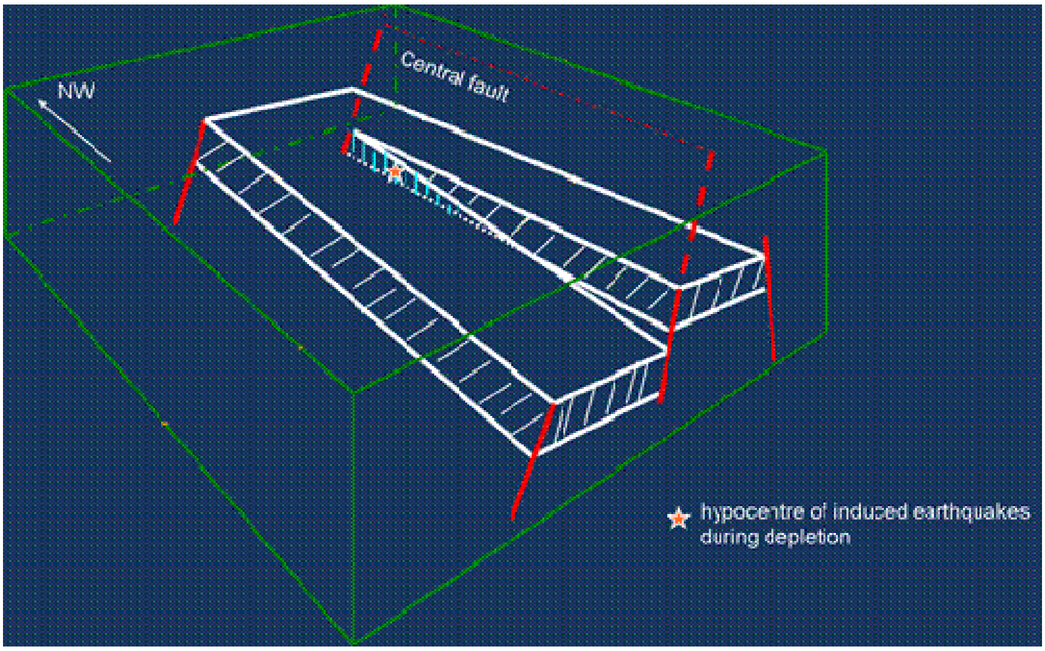

Figure 19 : Figure 4. Schematical geological model of the Rotliegend sandstone reservoir and location of induced seismicity during gas production. All events are located at the tip of the fault intersecting the reservoir blocks.

Table 1: Main characteristics and geomechanical parameters of the North Netherlands field case.

Reservoir	Rotliegend Slochteren Sandstone
Reservoirdepth	≈ 2000 - 2500m
Reservoirthickness	≈ 200m
Caprock	Zechsteincaprock: carbonates, shales and evaporites
In situ stresses	Extensional tectonic setting: S_{hmin}: 25 MPa S_{Hmax}: 44 MPa S_v: 49 MPa
Geomechanicalparameters	Reservoir rocks: E_{young}: 18GPa, ν: 0.2, porosity: 23% Caprock: E_{young}: 30GPa, ν: 0.3
Porosity, Permeability	varying≈300mDmD
Reservoirtemperature	86°C
Initial reservoir pressure & pressure drop depletion	≈ 230 bar; 200-220 bar
Mainfaults (dip/ strike)	Strike NW; Dip 65°; dip direction: SW&NE

Due to production of gas from both reservoir blocks, pore pressures in the reservoir blocks decreased from initially 230 bars to approximately 25 bars. After approximately 25 years of production and a pressure drop of 160 bars a seismic event of M=3.5 occurred, which was followed by 3 additional seismic events (M>3) during further depletion of the gasfield.

For this field a numerical geomechanical model has been constructed in the finite element software DIANA, in order to model the effects of both pore pressure changes, reservoir geometry and compartmentalization on the reactivation potential of the central fault. As the main objective of the analysis is the determination of the reactivation potential of the central fault, a simplified schematic disc-shaped model of the central fault plane with varying offset of both reservoir compartments has been constructed (see Figure 20). In this model stress paths on the sealing fault are monitored in order to analyse the fault reactivation potential and risk of induced seismicity during gas production.

Modelling results are shown in Figure 21 and Figure 22. Figure 21 shows the reactivated fault patches during depletion of the reservoir. Figure 22 presents the stress paths and development of shear and normal tractions on the fault plane during the depletion of the gas field. After several years of gas production the stress paths on the fault plane near the tip of the fault reach the Mohr Coulomb failure envelope and slip along the fault occurs. Both timing of fault reactivation and the location of reactivation at the tip of the fault are consistent with the observed induced seismic events.

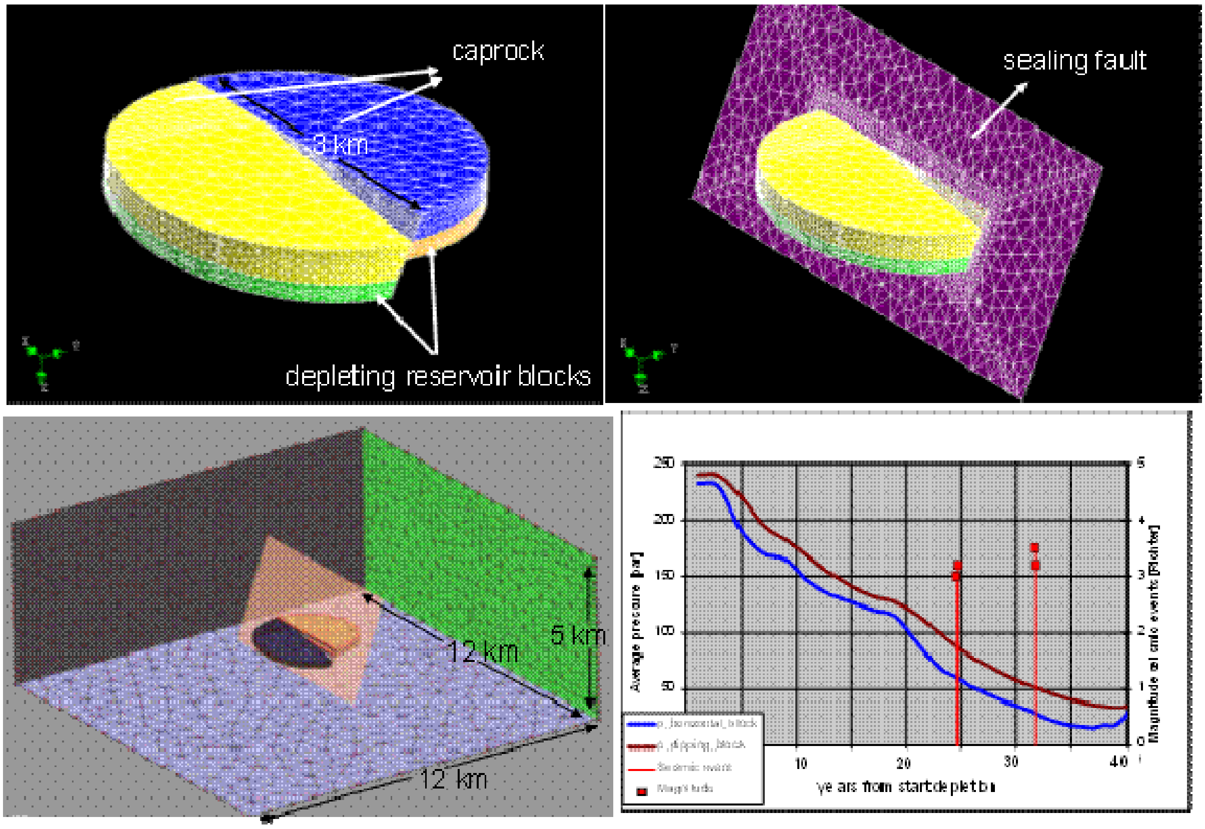
caprock
3 km
depleting reservoir blocks
sealing fault
12 km
5 km
12 km
250
200
150
100
50
Average pressure [bar]
5
4
3
2
1
0
Magnitude seismic events [Richter]
10
20
30
40
years from start depletion
p_horizontal_block
p_dipping_block
Seismic event
Magnitude

Figure 20 : Disc-shaped model in DIANA of a sedimentary sandstone reservoir (upper figures, reservoir is presented in green & orange) intersected by a partially sealing normal fault. Upper figures, caprock is shown in yellow and blue). The offset of the southwestern reservoir block and caprock varies along the strike of the fault. The north eastern reservoir block lies horizontally. Lower left graph shows the pore pressure evolution (blue line horizontal reservoir block, brown line dipping reservoir block) during gas production. Red squares present timing and magnitudes of seismic events.

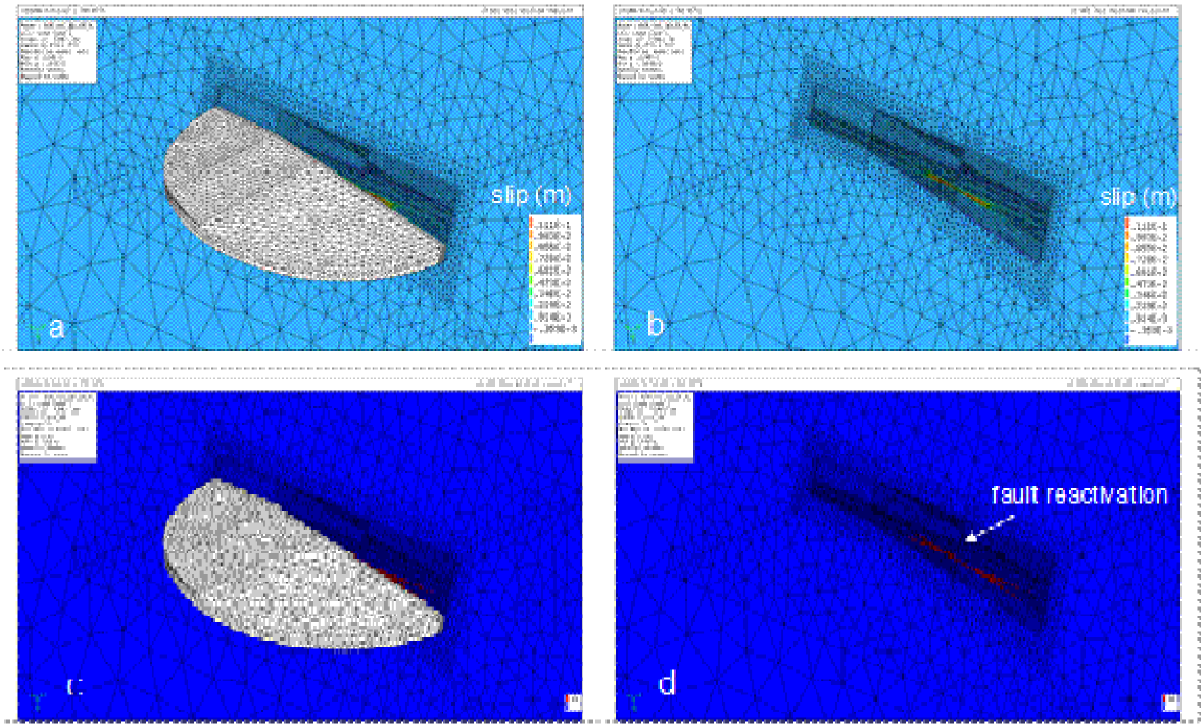

Figure 21 : a and b) Modelled fault slip during depletion of the gas field. Largest fault slip occurs at the tip of the fault, at the juxtaposition of the depleted reservoir blocks. This is consistent with the observed seismicity during depletion, which is localized at the tip of the fault. c and d) Area of reactivated fault patches presented in red.

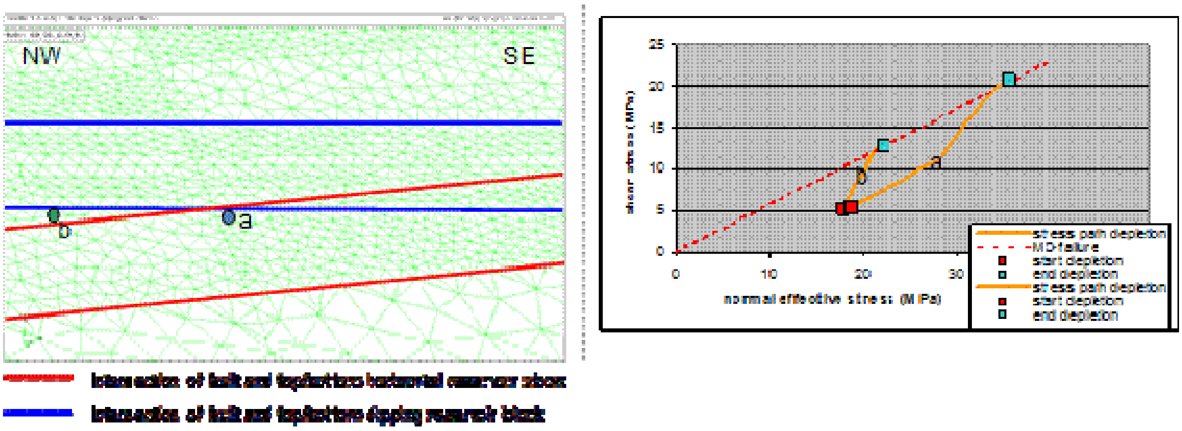

Figure 22 : Left: a) and b) are locations of monitoring points on the central fault plane. Both the intersection of the horizontal and the dipping reservoir block are projected on the faultplane. Right: Stress paths on central faultplane in the disc shaped model. Stress paths intersect the MC failure envelope of the fault during depletion, which means at the location of the monitoring points the fault is reactivated.

3.5. EGS IN COMPARTMENTALIZED SEDIMENTARY RESERVOIR – SOME PRELIMINARY CALCULATIONS

As already mentioned in section 39, pore pressures within the matrix of sedimentary reservoirs will be affected by flow from the fractures into the matrix. As opposed to EGS in impermeable crystalline rocks, significant poro-elastic effects and strains can occur in the matrix rocks between the fracture networks.

At present no data on EGS in compartmentalized reservoirs are available. However, general insights on the impact of reservoir compartmentalization on fault stability and induced seismic hazard for EGS in sedimentary reservoirs can be obtained from preliminary calculations using a schematic 2D numerical model of water injection in a sedimentary reservoir compartmentalized by a sealing fault.

In Figure 16 it was shown that in an extensional tectonic setting (with $S_v > S_{Hmax} > S_{hmin}$) , the differential stresses in the reservoir decrease during injection and increasing pore pressures. The stress path during injection can be either critical (convergent on the MC-line) or non-critical (diverging from the MC-line). Figure 23 shows the stress path on a critically oriented fault plane during the injection of water (pore pressure increase) in a reservoir (no arching or geometrical effects) in a compressive tectonic setting ($S_{Hmax} > S_{hmin} > S_v$). In this case stress paths during water injection converge towards the Mohr Coulomb failure line. A reverse stress regime promotes fault slip during injection. Whether or not fault reactivation and slip will occur depends on factors as the initial stress conditions (criticality), the gradient of the stress paths (defined by the depletion constant of the reservoir) and the strength of the fault (friction coefficient and cohesion). Next to the poro-elastic effect, the geometry of the reservoir is important. This effect is further investigated in a simplified 2D numerical model of a sandstone reservoir intersected by a (partially) sealing fault, constructed in the finite element program DIANA (see Figure 24).

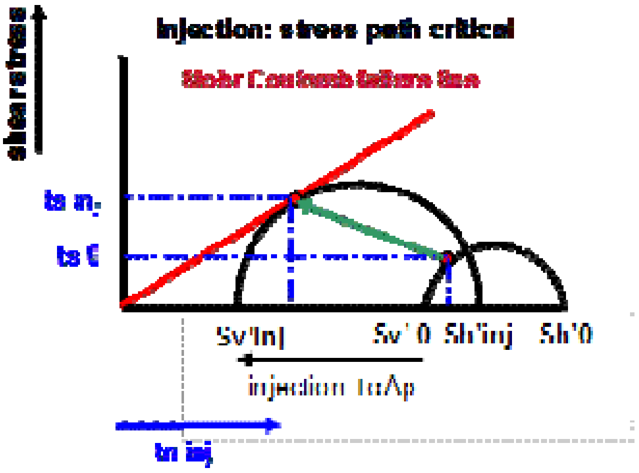

Figure 23 : Stress path on critically oriented fault plane during water injection (pore pressure increase) in a compressional tectonic setting ($S_{Hmax}>S_{hmin}>S_v$).

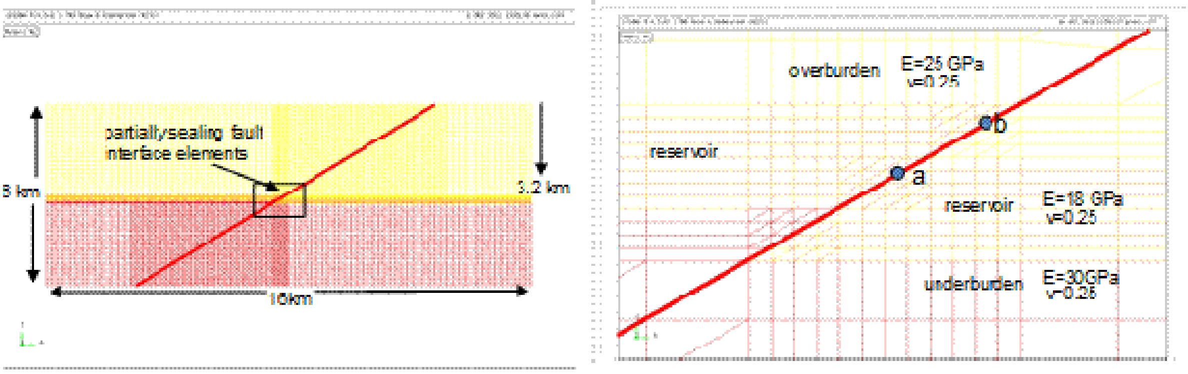

Figure 24 : Schematic 2D FE model of a 200m-thick sandstone reservoir at a depth of approximately 3km, intersected by a reverse fault. The fault is modelled by interface elements with a Mohr-Coulomb failure criterion (friction coefficient 0.6, no cohesion). The reservoir and the surrounding rocks are assumed elastic.

For this simplified reservoir geometry the effect of water injection on fault stability is analysed. It is assumed that due to the injection of water during EGS, the reservoir pressure in the compartments is increased by an average amount of 10MPa (3 cases are distinguished, injection in the higher reservoir compartment, in the lower compartment and in both compartments simultaneously). The effect of a pressure increase in the individual reservoir blocks is shown in Figure 25. Tractions on the fault plane are monitored at or close to the juxtaposition of the two reservoir blocks (locations of monitoring points are given in Figure 24 left). The stress paths show that, due to the increase in pore pressure, reactivation of the fault patches can occur at, or close to, the juxtaposition of the reservoir compartments.

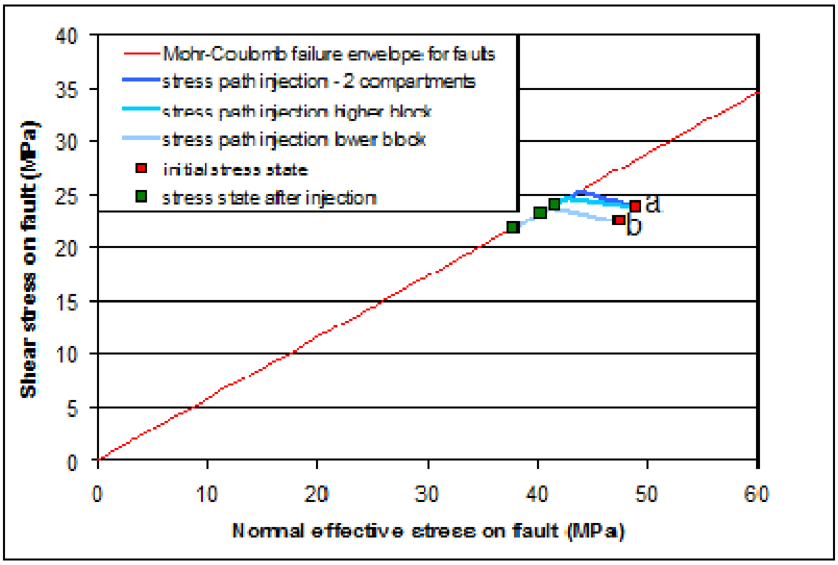

Figure 25 : Stress path in monitoring points a and b on fault plane due to pore pressure increase in individual reservoir compartments and both reservoir compartments simultaneously. For location of monitoring points see Figure 24.

3.6. CONCLUSIONS

Numerical modelling of the mechanisms of fault reactivation and induced seismicity during gas production from sedimentary reservoirs in the northern part of The Netherlands shows that poro-elastic effects due to pore pressure changes, compartmentalization and differential compaction can play an important role in the reactivation of faults during gas production. In contrast to EGS in low/impermeable crystalline (matrix) rocks, in EGS in sedimentary reservoirs pore pressure changes and related poro-elastic effects are also expected to occur in the matrix rocks between the fracture networks. Differential pore pressures development and differential deformation of reservoir matrix rocks will occur when large scale heterogeneities, such as sealing fault structures between reservoir compartments are present. Differential pore pressure evolution and differential deformation increase the risk of fault reactivation and induced seismicity. Whether or not faults will be reactivated due to pore pressure changes and deformation of the matrix rocks depends on numerous factors, amongst others the criticality of the stress state on the faults, the fault strength, the amount and extent of the pore pressure changes and the geomechanical properties of the matrix rocks. At present, no data on field cases of EGS in compartmentalized sedimentary reservoirs are available, but this preliminary analysis shows that for EGS in sedimentary reservoirs both the effects of pressure changes in the matrix rocks and the impact of large scale heterogeneities should be taken into account.

3.7. REFERENCES

Feigner, B., and Grasso, J.R. (1991). Relation between seismic source parameters and mechanical properties of rocks: a case study. Pure and Appl. Geophys., 137, 175-199.

Mulders, F.M.M (2003). Modelling of stress development and fault slip in and around a producing gas reservoir.PhD-thesis Technical University Delft.

Muntendam (2008).Bergermeer seismicity study.TNO-technical report 2008-U-R0871/B.

Van Eck (2006). Seismic hazard due to small-magnitude, shallow-source, inducedearthquakes in The Netherlands.Engineering Geology, 87, 105-121.

4. From geomechanical modeling to seismic hazard assessments

4.1. PREAMBLE

In this task 4.1, GEOWATT computed Coulomb Failure Stress changes derived from pore pressure changes. With a close collaboration between members of WP5 and WP3, these stress changes computations are used for predicting a reservoir seismic response.

4.2. INTRODUCTOIN

Although good progress has been achieved in numerical modeling of the hydro-mechanical response of geothermal reservoirs to stimulation, only few conclusions regarding the seismic risk of different injection approaches could be made. To solve this issue, we use a hydro-mechanical finite-element code to compute changes of Coulomb Failure Stress derived from changes of pore pressure. A statistical rate-and-state approach is then applied to translate stress changes to a prediction of the seismic response of the reservoir. Our model is applied to different stimulation scenarios.

This work is a close collaboration between members of WP5 (A. Hakimhashemi andO. Heidbach, GFZ Potsdam), WP4 (M. Schoenball, GEOWATT AG) and WP3 (A. Zang, GFZ Potsdam) in an effort to strengthen the exchange among the workpackages and to join ideas from different perspectives.

4.3. GEOMECHANICAL MODELLING

Our numerical modelling is based on the hydraulic finite element code FRACTure (Kohl et al, 1995) which is coupled to a 3D stochastic fracture network and the code HEX-S to incorporate fracture mechanical behavior (Kohl &Mégel, 2007). This package has previously been successfully applied to predict the hydraulic and seismic behaviour of the stimulation of GPK4 at the Soultz-sous-Forêts geothermal site (Kohl &Mégel, 2007).

The output of this geomechanicalmodelling is spatio-temporal changes of pore fluid pressure in the 3D reservoir. These can be converted to changes of Coulomb Failure Stress, which are input data to the subsequently applied Rate-and-State model

4.4. RATE-AND-STATE MODEL

The Rate-and-State model (Dieterich, 1994) is used to translate changes of stress to rates of seismicity. The rate of seismicity R isgiven by :

$$R = \frac{r}{\gamma \dot{\tau}_r},$$

where r is the rate of background seismicity, $\dot{\tau}_r$ is the shear stressing rate and γ is the state variable given by:

$$\gamma = \left(\gamma_0 - \frac{1}{\dot{\tau}}\right)\exp\left(-\frac{\dot{\tau}t}{A\sigma}\right) + \frac{1}{\dot{\tau}},$$

wheret is time and Aσis the major free parameter comprised of the apriori unknown constitutive fault parameter A and normal stress on the fault σ. To calculate the seismic response of the reservoir changes of seismic rate are integrated over the whole reservoir volume.

4.5. RESULTS

4.5.1. Application to the Stimulation of GPK4 at Soultz-sous-Forêts (France)

The above described model is applied to the stimulation of GPK4 in the year 2004. The injection rates of the stimulation where used as input for the geomechanical model.

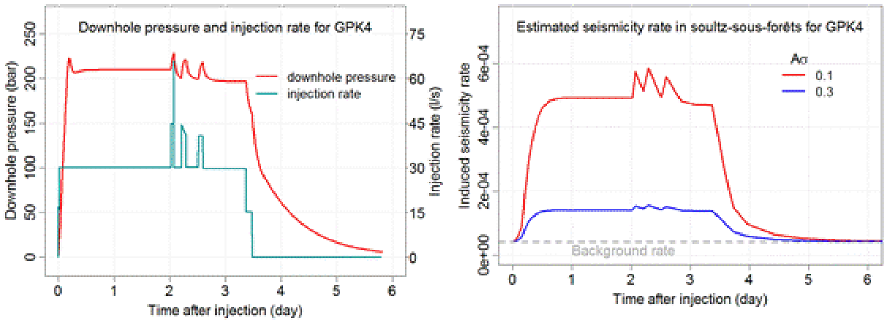

(a) (b)

Figure 26 : (a) Injection rates during the GPK4 stimulation and downhole pressure simulated with HEX-S. (b) Seismicity rates converted from pore pressures for two Aσ.

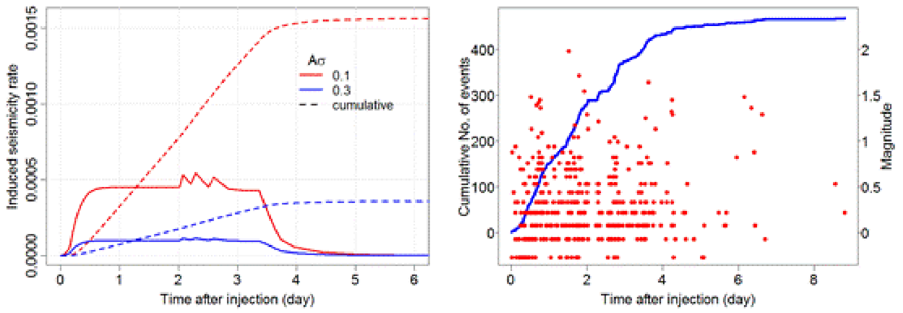

(a) (b)

Figure 27 : (a) Estimated seismicity rates and cumulative rates, compared to (b) observed seismicity during the stimulation of GPK4. The simulated temporal evolution of cumulative seismicity rates are in good agreement with the observation.

4.5.2. Different stimulation scenarios

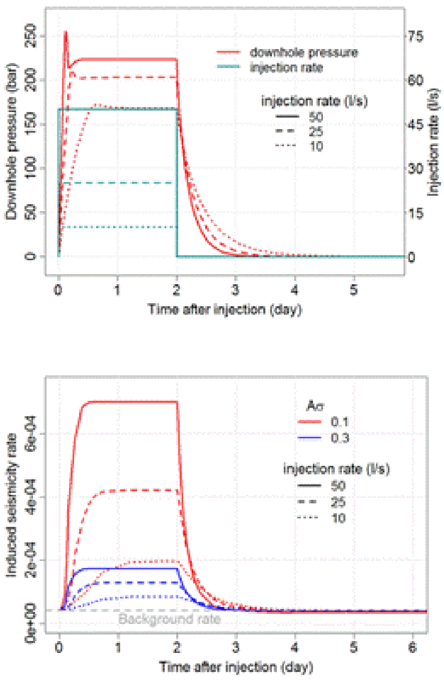

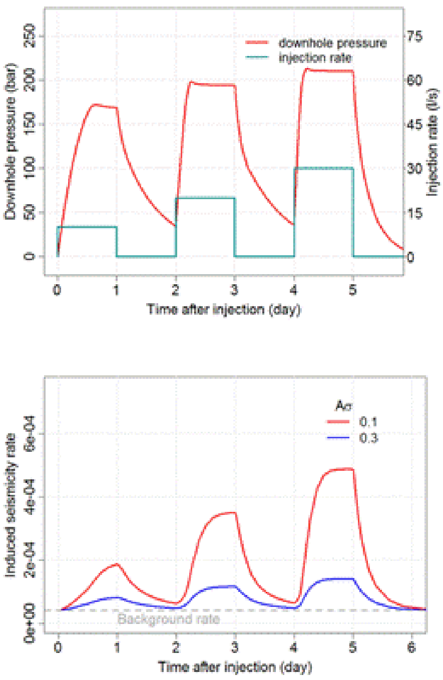

Constant injection of 10, 25 and 50 l/s

Periodic injection

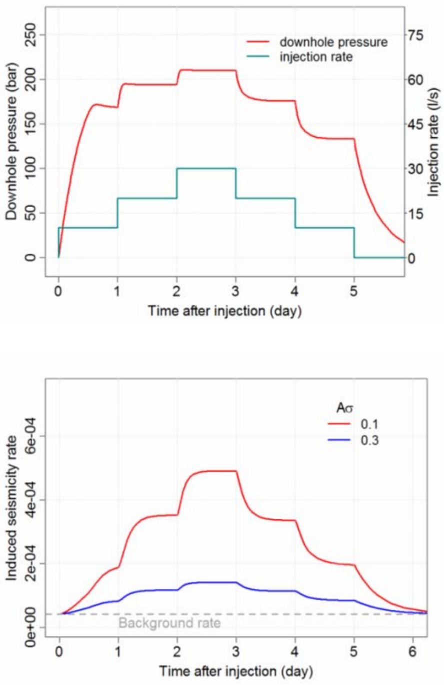

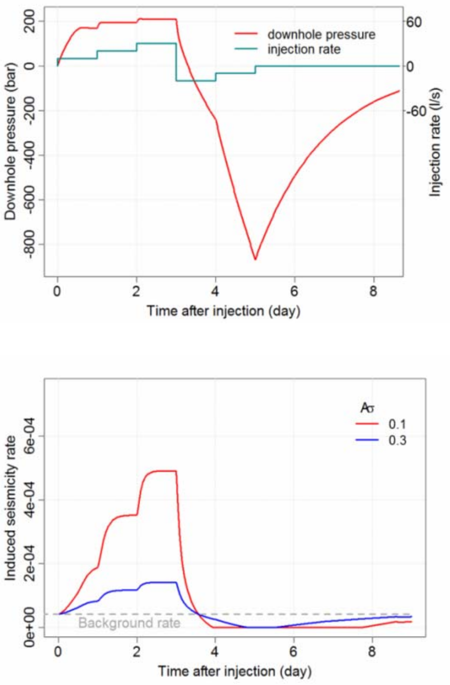

Step-wise increase and decrease of injection rate

Step-wise increase of injection and production after shut-in

4.5.3. Interpretation

- The seismicity rate is different from the downhole pressure in shape, but it directly follows the pressure.

- The seismicity rate is sensitive to the injection rate and consequently to the downhole pressure.

- This approach only estimates the seismicity rate directly induced by the change in pore pressure, but not the aftershocks or fracture interactions. The next step is to combine this method with an additional model like ETAS.

- This approach is not able to estimate the maximum magnitude.

4.6. CHALLENGES

- Length of time intervals in Rate-and-State model

- Number of fractures in a certain area

- Modelling aftershocks and fracture interaction effects (ETAS model)

- Considering parameter uncertainties

4.7. REFERENCES

Dieterich, J., 1994, A constitutive law for rate of earthquake production and its application to earthquake clustering. J. Geophys. Res., 99: 2601-2618.

Kohl, T., Evans, K.F., Hopkirk, R.J. and Rybach, L., 1995, Coupled hydraulic, thermal and mechanical considerations for the simulation of hot dry rock reservoirs. International Journal of Rock Mechanics and Mining Sciences and Geomechanics Abstracts, 33: 130A-130A.

Kohl, T. and Megel, T., 2007, Predictive modeling of reservoir response to hydraulic stimulations at the European EGS site Soultz-sous-Forets.International Journal of Rock Mechanics and Mining Sciences, 44: 1118-1131.

5. Time-dependent variation of pore pressure with a fluid dynamic approach

5.1. PREAMBLE

The role of INGV in Task 4.1 aims at studying the time-dependent variations of pore pressure in the seismic volume with a fluid-dynamical approach and the computation of Coulomb stress changes.

5.2. INTRODUCTION

All the mining and geothermal activities implying fluid injection and withdrawal have the potential to induce seismicity, whose tolerable level of magnitude depends essentially from the closeness to dense urban settlements (eg. Majer at al., 2007, and references therein). Such mechanisms of induced seismicity, despite several decades of experience, are not known in details, preventing till now an effective assessment and/or mitigation.

5.3. METHOD

The cause of induced seismicity must be obviously ascribed to the pressure changes in the rocks induced by fluid injection or withdrawal. However, the pressure change is not easily linked to the seismicity occurrence, whereas the most obvious parameter to describe the link with seismicity is the Coulomb stress (Stein et al., 1992). In order to understand the relation between the fluid injection/withdrawal activities and the seismicity, we used a modeling approach to the general problem consisting in the simulation of fluid injection/withdrawal at depth, in a given reservoir model, and computing the induced Coulomb stress changes. In the framework of the Coulomb criterion, failure on a fault occurs when the applied Coulomb stress overcomes a strenght threshold. Coulomb stress on a given fault plane is defined as the sum of the shear stress and a fraction of the normal stress, taken positive in the sense of fault opening: $\sigma_f = \tau_s + \mu(\sigma_n\text{-}P)$,where τ_s is the shear stress, σ_n is the normal stress, μ is the friction coefficient and P is the pore pressure (Jaeger & Cook, 1979). In our approach, we compute Coulomb stress changes due to fluid injection/withdrawal from the induced pressure and temperature changes; they are obtained through a thermo-fluid-dynamical approach based on the THOUGH2 algorithm (Pruess, 1991). Successively, the incremental stress tensor is evaluated by using the finite element code COMSOL (see also Hurwitz et al., 2007 and Troiano et al., 2011).

The method we developed consists of a two-step procedure. In the first step, injection or withdrawal of water is simulated by the numerical algorithm THOUGH2, by computing pressure and temperature changes in the volume. This code allows computing the mass and heating exchange related to multidimensional flows of multiphase (gas and liquid) mixtures of many components within a porous medium of assigned permeability (Pruess 1991; Pruess et al. 1999). It assumes local equilibrium between fluid and rock matrix, through the direct discretization of the balance equations for mass and energy describing the thermodynamic conditions of the system in their integral form, in a scheme called integral finite difference method (Edwards 1972). Once the thermodynamic evolution of the modeled physical domain is simulated by numerical approximation, we use the obtained solution for pressure/temperature change as a source term to estimate the incremental stress tensor in the elastic matrix. The incremental stress tensor is computed by using a finite element model. For such a computation, the volume has to be subdivided into a dense mesh of volume elements and a denser sampling has to be used in the neighborhoods of the injection/withdrawal position. Figure 28 shows the different meshes used for the thermo-fluid-dynamical (left) and the elastic (right) modeling. At each element of the elastic mesh, the pressure and temperature changes, computed by THOUGH2, are used as individual sources, whose summation is used to compute the incremental stress tensor in the whole volume. In the developed process, the assumption that the change in stress has no effect on permeability, porosity or fluid flow is implicit. Such a one-way coupling approach (that is, from thermodynamics to alstic stress but not vice versa) is normally adopted in such simulations (Hurwitz et al. 2007), and differs from a complete and much more cumbersome thermo-poroelastic approach, in which volume deformation affects in turn the porosity and hence the permeability of the system. Once the complete field of stress changes is computed, Coulomb stress changes on a given fault plane in the volume can be obtained by the formula:

$$\Delta\sigma_f = \Delta\tau_s + \mu(\Delta\sigma_n - \Delta P)$$

where$\Delta\tau_s$ is the shear stress change, $\Delta\sigma_n$is the change of stress normal to the plane, $\Delta P$is the pore pressure change and μ is the friction coefficient. The Coulomb stress changes are computed on the most favourably oriented fault planes, i.e., at each grid point, the one on which the total Coulomb stress, including the tectonic stress plus the incremental stress due to withdrawal/injection of water, is maximum.

5.4. RESULTS

Such method has been applied to simulate both injection and withdrawal. The obtained results, for the two different cases, are summarized, respectively, in Figure 29 and Figure 30. In the two cases, injection/withdrawal of water for 15 days, at a rate of 50 l/s is simulated, in a rock volume with permeability 10^{-16} m^2, with density 2600 kg/m^3 and thermal conductivity 2.0 W/m°C. From Figure 29, it is evident that the pressure changes induced by water injection and withdrawal are quite similar apart from the sign. The Coulomb stress patterns show, on the contrary, strong differences. The discriminating factor is that, for withdrawal, the normal component in the Coulomb stress equation is decreased, thus stabilizing the fractures, and the only positive effect occurs where additional shear stress is generated. Water injection, on the contrary, increases the normal component in the volume around, thus destabilizing the fractures at a much larger extent. This appears to be the reason why high pressure water injection at EGS sites poses a much higher seismic hazard, with respect to simple geothermal exploitation of hydrothermal systems or, equivalently, to oil/gas withdrawal.

The rock parameters used in this preliminary test are appropriate for the area of Soultz-sous-forets, in France, where the first EGS geothermal plant has been operated (Baria et al., 2004). In the following, we apply our method to simulate Coulomb stress changes due to stimulation of two wells at Soultz, and compare our results with seismicity observed at several times during the period of stimulation (Cuenot et al., 2008).

Our simulation has been calibrated to roughly simulate the simultaneous stimulation of the GPK2 and GPK3 wells performed in 2003, as reported by Baria et al. (2004). A simplified but realistic injection function has been used for the simulation (see Figure 30). Again, a homogeneous medium with the same rock parameters used before has been considered. The initial conditions are shown in Figure 29. The entire water injection cycle is simulated in both GPK3 (blue line) and GPK2 (red line) wells. Starting from day 0, cold water is injected in GPK3 well while GPK2 is shut off. On day 5 the GPK2 is switched on and the injection is performed in both the wells. Successively, on day 8, GPK2 is shut off again and the injection rate of GPK3 is decreased and remains constant till the day 12, when also GPK3 is shut off.

The results obtained for this simulation are shown in Figure 31 (for the pressure changes) and Figure 32 (for the coulomb stress changes). Figure 33 and Figure 34show the comparison between computed maximum Coulomb stress changes and observed seismicity in the considered periods. In particular, Figure 33 shows the Coulomb stress changes at the day 5 and the seismicity occurred in the period 0-5 days. Figure 34 shows Coulomb stress changes computed between 12 and 16 days after the start of the stimulation cycle, i.e. between stimulation periods 5 and 6; coherently, seismicity occurred during the two periods is shown.

5.5. CONCLUSIONS

Our results show extremely good agreement between modeled Coulomb stress changes and observed seismicity. Although we show here such agreement only for initial and final stimulation periods, it remains exceptionally good also in the intermediate ones. On the grounds of our results, it appears clear that the main causes of induced seismicity during stimulation are the Coulomb stress changes generated by water injection. In fact, the resulting agreement between modeled stress changes and seismicity appears very good also if the used model is very simple and neglects several complications of the real situation. Among the neglected effects, we should list the increase of permeability due to earthquake occurrence; it should in turns enlarge progressively the seismic volume, while decreasing the pressure at the well’s bottom and in its neighboring (pressure is inversely related to the permeability). This effect can be anyway simulated by changing the permeability values during the time steps of simulation, following some empirical relation between earthquake occurrence and permeability. We are actually trying to add such permeability increase effect, and furthermore to add the additional Coulomb stress changes due to the induced earthquakes.

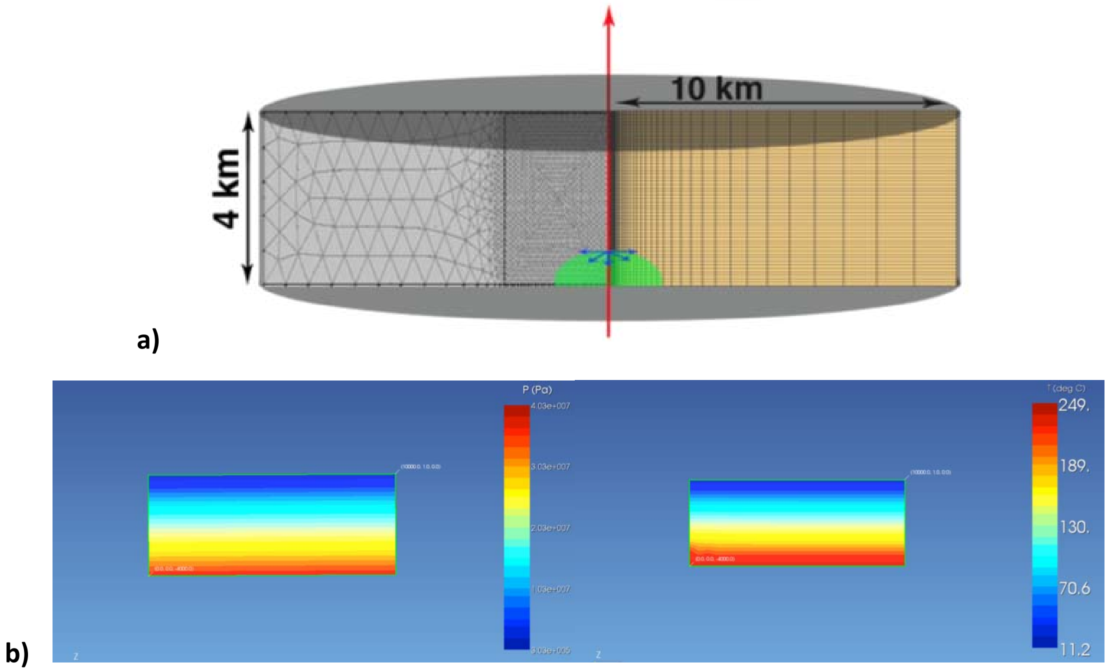
4 km
10 km
a)
b)
P (Pa)
4.03e+007
3.03e+007
2.03e+007
1.03e+007
3.03e+005
T (deg C)
249.
189.
130.
70.6
11.2
z
z

Figure 28 :Theoretical model meshes; a) Axial symmetric model domains used for thermo-fluid dynamical modeling and for surface deformation computation. Right side: finite-difference computational domain for thermo-fluid dynamical modeling. The green part of the model is characterized by a permeability 10^{-14} m^2, while the external part has a permeability 10^{-16} m^2; b) Initial conditions for Pressure (P) and Temperature (T), at the top of the model, Temperature and Pressure are fixed at atmospheric values, while on the bottom the pressure is lithostatic, with average density r=2500 kg/m^3, while the Temperature is fixed at a value of 300°C.

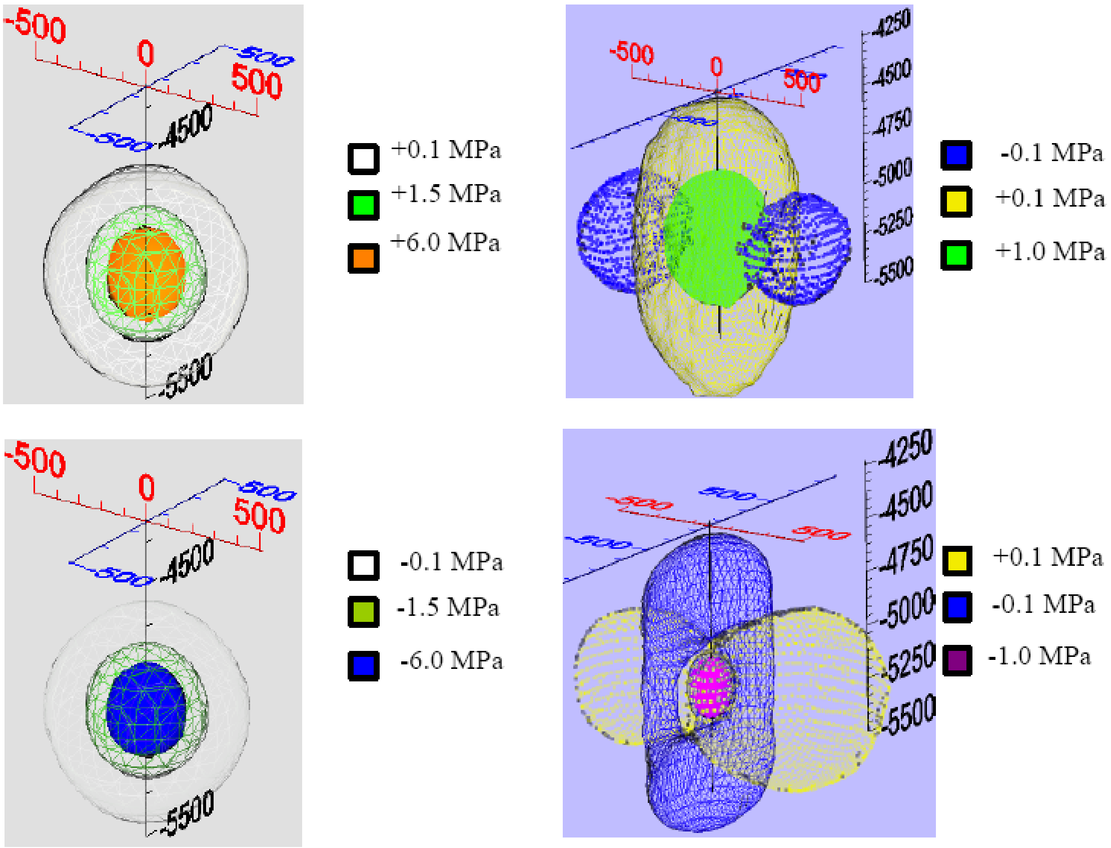
-500
0
500
500
-500
-4500
-5500
+0.1 MPa
+1.5 MPa
+6.0 MPa
-4250
-4500
-4750
-5000
-5250
-5500
-0.1 MPa
+0.1 MPa
+1.0 MPa
-0.1 MPa
-1.5 MPa
-6.0 MPa
+0.1 MPa
-0.1 MPa
-1.0 MPa

Figure 29: Pressure changes (left) and maximum Coulomb stress changes (right) resulting from injection (upper) and withdrawal (lower) of 50 l/s of water, at 5 km of depth, in a homogeneous medium with permeability 10^{-16} m^2. It is evident that the pressure changes induced by water injection and withdrawal are quite similar apart from the sign. The Coulomb stress patterns show, on the contrary, strong differences. The discriminating factor is that, for withdrawal, the normal component in the Coulomb stress equation is decreased, thus stabilizing the fractures, and the only positive effect occurs where additional shear stress is generated. Water injection, on the contrary, increases the normal component in the volume around, thus destabilizing the fractures at a much larger extent.

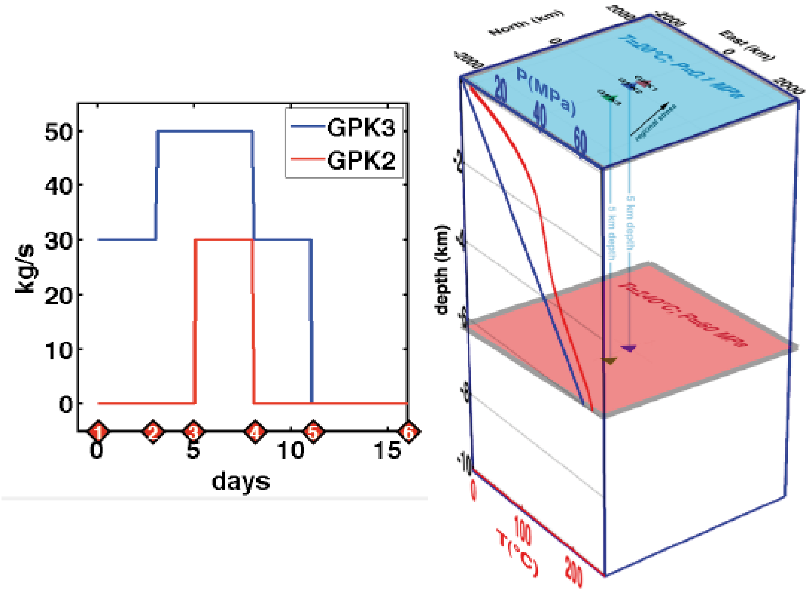

Figure 30 : Simplified stimulation functions for GPK2 and GPK3 Soultz-sous-Forêts wells (left), and sketch of simulation volume with wells positions and pressure/temperature initial conditions (right).

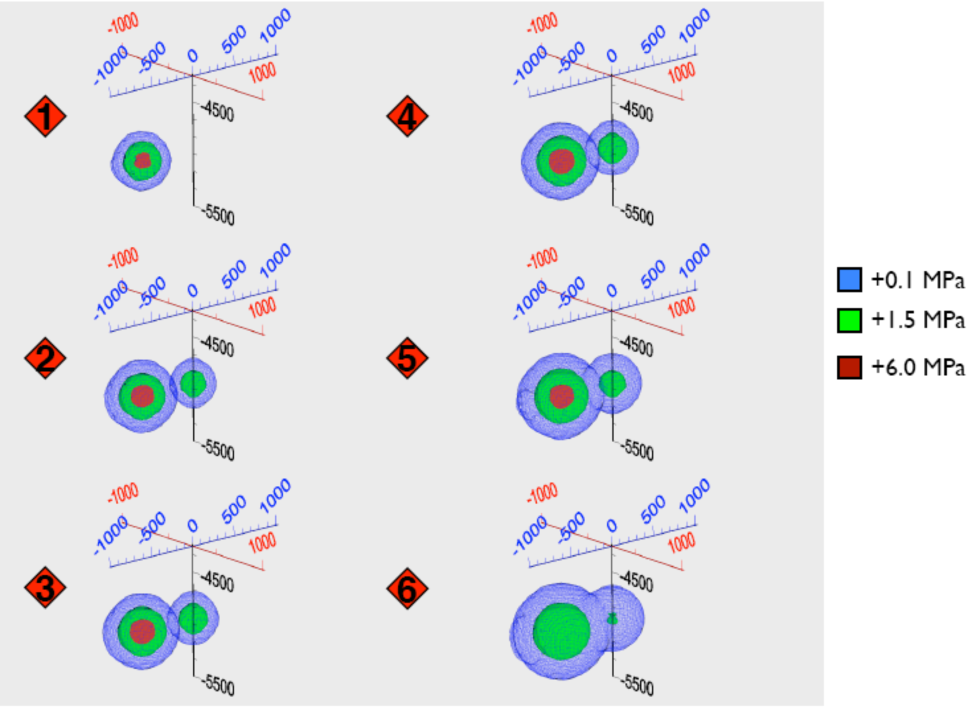
1
2
3
4
5
6
-1000
-500
0
500
1000
-4500
-5500
🟦 +0.1 MPa
🟩 +1.5 MPa
🟥 +6.0 MPa

Figure 31:Estimated pressure changes for the different phases of the injection experiment described in Figure 30 Numbers from 1 to 6 refer to the times of the stimulation cycle shown in Figure 30.

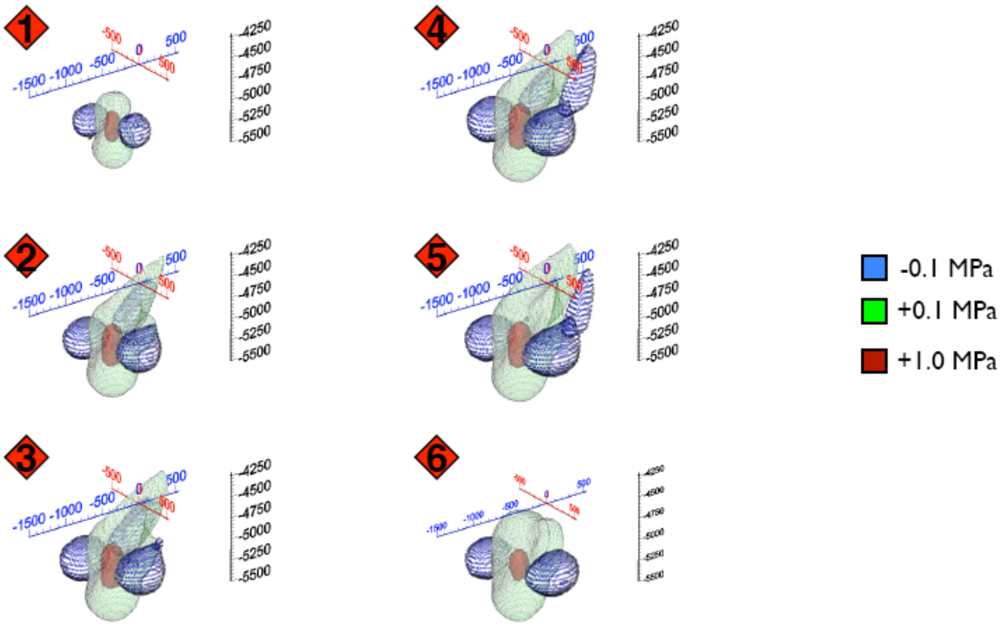
1
2
3
4
5
6
-1500 -1000 -500
-500
0
500
500
-4250
-4500
-4750
-5000
-5250
-5500
🟦 -0.1 MPa
🟩 +0.1 MPa
🟥 +1.0 MPa

Figure 32 :Maximum Coulomb stress changes for the different phases of the injection experiment described in Figure 30.

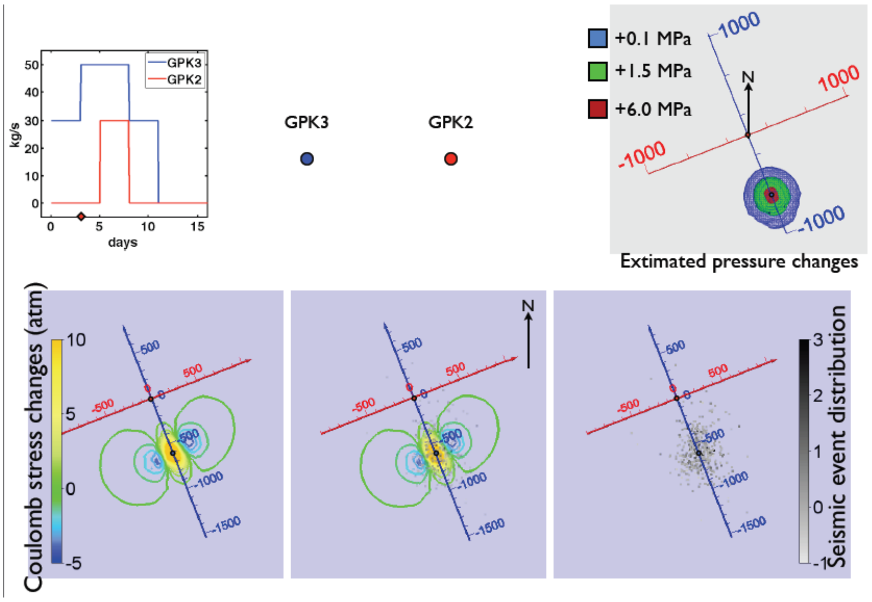

Figure 33:Results (projected on map at 5000 m of depth) for pressure and maximum Coulomb stress changes after the first three days of stimulation of GPK3 well. The reference system is rotated along the direction passing between the two wells.

Coulomb stress changes are also compared with seismicity occurred in the period 0-3 days. Note the good agreement between positive stress changes and seismic areas.

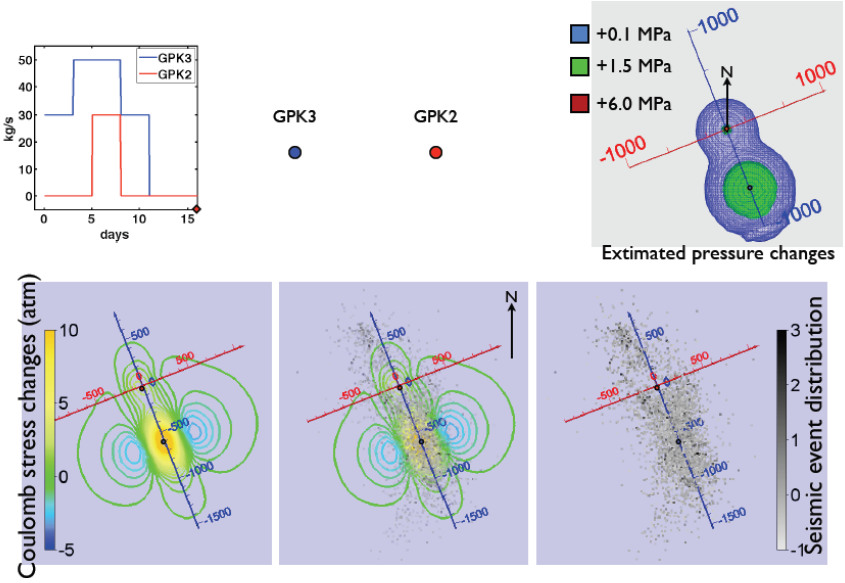

Figure 34: Results (projected on map at 5000 m of depth) for pressure and maximum Coulomb stress changes after the end of stimulation cycle of the two wells. Coulomb stress changes are also compared with seismicity occurred in the period 0-3 days. Note, also in this case, the good agreement between positive stress changes and seismic areas.

5.6. REFERENCES

Baria, R., Michelet, S., Baumgärtner, J., Dyer, B., Gerard, A., Nicolls, J., Hettkamp, T., Teza, D., Soma, N., Asanuma, H., Garnish, J., Megel, T. (2004), “Microseismic monitoring of the world’s largest potential HDR reservoir,” Proceedings, 29th workshop on Geothermal Reservoir Engineering, Stanford University, California, 26-28 January 2004.

Cuenot, N., Dorbath, C., Dorbath, L. (2008). Analysis of the microseismicity induced by fluid injection at the EGS Site of Soultz-sous-Forets (Alsace, France): Implications for the characterization of the Geothermal Reservoir Properties. Pure and Applied Geophys., 165, 797-828.

Hurwitz, S., Christiansen, L. B. & Hsieh, P. A. (2007). Hydrothermal fluid flow and deformation in large calderas: Inferences from numerical simulations. J. Geophys. Res. 112(B2): 1-16.

Jaeger, J. C., and Cook, N. G. W. (1979). Fundamentals of Rock Mechanics (Third edition ed.). London: Chapman and Hall.

Majer, E.L., Baria, R., Stark, M., Oates, S., Bommer, J., Smith, B., and Asanuma, H., 2007, Induced seismicity associated with enhanced geothermal systems: Geothermics, v. 36, p. 185-222.

Pruess, K. (1991). TOUGH2 - A General Purpose Numerical Simulator for Multiphase Fluid and Heat Flow. L. B. L. Report. Berkeley, CA. LBL-29400.

Stein, R. S., King, G. C. P., and Lin, J. (1992). Change in failure stress on the southern San Andreas fault system caused by the 1992 Magnitude = 7.4 Landers earthquake, Science, 258, 1328-1332.

Troiano, A., Di Giuseppe, M.G., Petrillo, Z., Troise, C. and De Natale, G. (2011). Ground deformation at calderas driven by fluid injection: modelling unrest episodes at CampiFlegrei (Italy). Geophys. J. Intern., in press.

GEISER